The ultraluminous state revisited: fractional variability and spectral shape as diagnostics of super-Eddington accretion

Andrew D. Sutton,[1]⋆ Timothy P. Roberts[1] and Matthew J. Middleton[1,2]

[1]*Department of Physics, University of Durham, South Road, Durham DH1 3LE, UK*
[2]*Astronomical Institute Anton Pannekoek, Science Park 904, NL-1098 XH Amsterdam, the Netherlands*

ABSTRACT

Although we are nearing a consensus that most ultraluminous X-ray sources (ULXs) below $10^{41}\,\mathrm{erg\,s^{-1}}$ represent stellar mass black holes accreting in a super-Eddington 'ultraluminous' accretion state, little is yet established of the physics of this extreme accretion mode. Here, we use a combined X-ray spectral and timing analysis of an *XMM–Newton* sample of ULXs to investigate this new accretion regime. We start by suggesting an empirical classification scheme that separates ULXs into three classes based on the spectral morphologies observed by Gladstone et al.: a singly peaked *broadened disc* class, and two-component *hard ultraluminous* and *soft ultraluminous* regimes, with the spectra of the latter two classes dominated by the harder and softer component, respectively. We find that at the lowest luminosities ($L_{\mathrm{X}} < 3 \times 10^{39}\,\mathrm{erg\,s^{-1}}$) the ULX population is dominated by sources with broadened disc spectra, whilst ULXs with two-component spectra are seen almost exclusively at higher luminosities, suggestive of a distinction between ∼Eddington and super-Eddington accretion modes. We find high levels of fractional variability are limited to ULXs with soft ultraluminous spectra, and a couple of the broadened disc sources. Furthermore, the variability in these sources is strongest at high energies, suggesting it originates in the harder of the two spectral components. We argue that these properties are consistent with current models of super-Eddington emission, where a massive radiatively driven wind forms a funnel-like geometry around the central regions of the accretion flow. As the wind provides the soft spectral component this suggests that inclination is the key determinant in the observed two-component X-ray spectra, which is very strongly supported by the variability results if this originates due to clumpy material at the edge of the wind intermittently obscuring our line-of-sight to the spectrally hard central regions of the ULX. The pattern of spectral variability with luminosity in two ULXs that straddle the hard/soft ultraluminous regime boundary is consistent with the wind increasing at higher accretion rates, and thus narrowing the opening angle of the funnel. Hence, this work suggests that most ULXs can be explained as stellar mass black holes accreting at and above the Eddington limit, with their observed characteristics dominated by two variables: accretion rate and inclination.

Key words: accretion, accretion discs – black hole physics – X-rays: binaries – X-rays: galaxies.

1 INTRODUCTION

Ultraluminous X-ray sources (ULXs) are point sources of X-rays, with luminosities at or in excess of the Eddington limit for a typical Galactic black hole of mass $\sim 10\,\mathrm{M_\odot}$ ($\gtrsim 10^{39}\,\mathrm{erg\,s^{-1}}$). They are located outside of the nucleus of their host galaxies, so cannot be powered by accretion on to supermassive black holes (SMBHs; $> 10^5\,\mathrm{M_\odot}$). Whilst accretion on to a population of intermediate-mass black holes (IMBHs; Colbert & Mushotzky 1999; $10^2 \lesssim M_{\mathrm{BH}} \lesssim 10^4\,\mathrm{M_\odot}$) remains a possible explanation for a subset of some of the brightest ULXs (e.g. Farrell et al. 2009; Sutton et al. 2012), it is unlikely to be the case in the majority of the population. The evidence for this is varied; notably if all ULXs contained IMBH primaries, it would imply an unfeasibly high IMBH formation rate in star-forming galaxies (King 2004); and a population of IMBHs alone is inconsistent with the break at $\sim 2 \times 10^{40}\,\mathrm{erg\,s^{-1}}$ in the luminosity function of point X-ray sources in star-forming galaxies (e.g. Swartz et al. 2004; Mineo, Gilfanov & Sunyaev 2012). Indeed, this is strongly supported by the detection

⋆ E-mail: andrew.sutton@durham.ac.uk

of both a soft excess and high energy curvature in a number of high-quality *XMM–Newton* ULX observations (e.g. Roberts et al. 2005; Gonçalves & Soria 2006; Stobbart, Roberts & Wilms 2006; Gladstone et al. 2009; Miyawaki et al. 2009), which are inconsistent with these sources being in known sub-Eddington accretion states. Instead, the majority of ULXs are likely powered by accretion on to fairly typical stellar remnant black holes. In this case, many may be classic stellar mass black holes (sMBHs; $M_{BH} < 20\,M_\odot$; Feng & Soria 2011), which would need to be accreting at super-Eddington rates to produce the observed luminosities. However, this requirement could be relieved in some ULXs if they instead contain slightly larger massive stellar remnant black holes (MsBHs; $20 < M_{BH} < 100\,M_\odot$; Feng & Soria 2011), which may form in regions of low metallicity (Zampieri & Roberts 2009; Belczynski et al. 2010; Mapelli et al. 2010).

Stobbart et al. (2006) demonstrated that some of the highest quality *XMM–Newton* ULX spectra were well represented by a model consisting of two thermal (or thermal-like) components, different to the spectra shown by typical sub-Eddington black holes, suggestive of a new, super-Eddington 'ultraluminous' accretion state (Roberts 2007). Gladstone et al. (2009) then investigated the physics of the highest quality *XMM–Newton* ULX spectra in more detail, and in doing so identified three spectral types of ULXs, which they speculated could be placed into a sequence with increasing accretion rate. In their interpretation, at around the Eddington limit ULXs appear with broad disc-like spectra; as the accretion rate becomes more super-Eddington a two-component spectrum emerges, initially peaking in the higher energy component; and, at the highest super-Eddington accretion rates the balance of the two components shifts, and the ULX appears instead with its peak at the softer end of the 0.3–10 keV spectrum. Here, we refer to these three ultraluminous spectral regimes as the 'broadened disc', 'hard ultraluminous' and 'soft ultraluminous' states, respectively (see Fig. 1 for an illustration of these spectra). Initially Gladstone et al. (2009) interpreted the hard and soft spectral components as a cool, optically thick corona around the inner disc, and the unobscured outer disc emission, respectively, however more recent work has refined this. The hard spectral component may indeed originate in a Comptonizing corona around the inner regions of the accretion disc; similarly, the consistently super-Eddington Galactic black hole binary GRS 1915+105 (Done, Wardziński & Gierliński 2004) also requires cool Comptonization (Zdziarski et al. 2001; Middleton et al. 2009; Ueda, Yamaoka & Remillard 2009). Alternatively, the hard emission could instead be coming directly from the hot inner disc (Middleton et al. 2011a), with its spectral shape plausibly due to a large colour correction (Kajava et al. 2012). The soft component likely originates in the photosphere at the base of a massive radiatively driven wind, as is expected to occur in black holes that are close to or exceeding Eddington-limited accretion (Poutanen et al. 2007); this is consistent with the apparent cooling of the soft component as its luminosity increases ($L \propto T^{-3.5}$; Kajava & Poutanen 2009).[1] So, given this revision in our understanding of the nature of the two components, it is pertinent to ask whether the different regimes really are a function of accretion rate alone, or whether they might instead depend on other characteristics of the ULX.

One way to make progress in this regard is to ask the question: how do the observed short-term variability properties of ULXs relate to the spectral regimes seen in the ultraluminous state? The
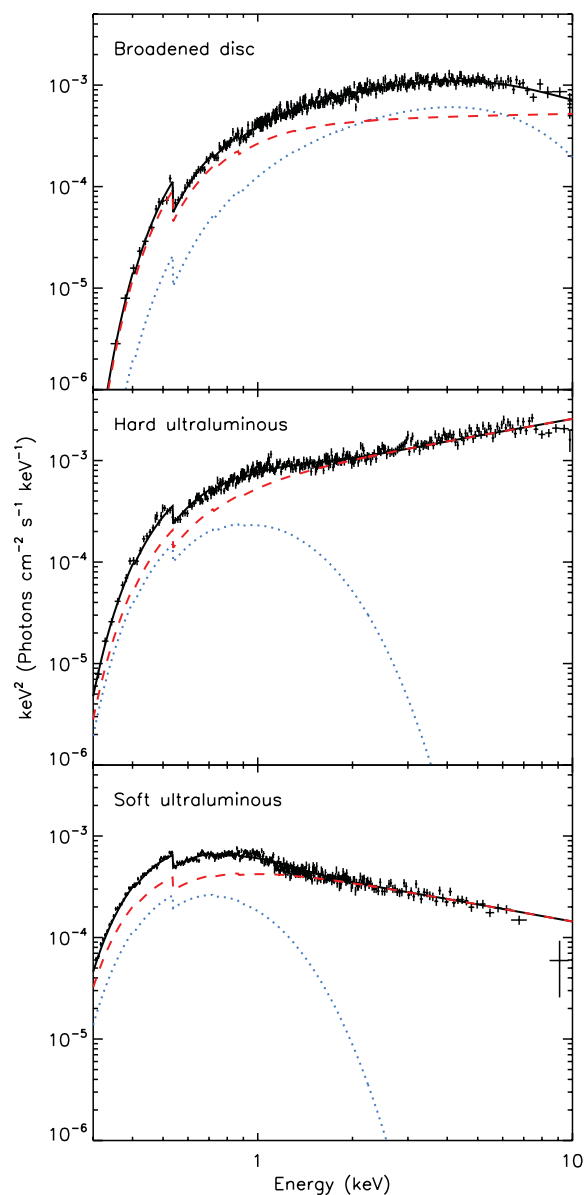
[1] Other scenarios exist that can also produce the observed luminosity–temperature relation, e.g. Soria (2007).

Figure 1. Example spectra from observations of different ULXs exhibiting each of the three spectral types. From top to bottom they are: broadened disc – observation 0405090101 of NGC 1313 X-2; hard ultraluminous – observation 0200980101 of Ho IX X-1; soft ultraluminous – observation 0653380301 of NGC 5408 X-1. For clarity, data are rebinned to 10σ significance and only EPIC PN detections are shown. The contributions from each of the components in the best-fitting absorbed MCD (blue dotted line) plus power-law (red dashed line) model are shown. The subtle spectral turnover indicative of ultraluminous state spectra is clearly seen in the data in the lower two panels, falling below the power-law tail whose slope is predominantly set by the data between ∼2 and 6 keV.

extended thermal emission from the radiatively driven wind should be intrinsically stable over short time periods, given it originates in an optically thick region. However, the smaller scale of the inner emission region means that it could vary, although this is not the case in many ULXs which instead are observed to have suppressed variability (Heil et al. 2009), possibly due to the stabilizing effect of advection on the disc structure (Abramowicz et al. 1988). Despite this, a few ULXs have been reported as displaying short time-scale variability, including reported quasi-periodic variability in M82 X-1

(Strohmayer & Mushotzky 2003), NGC 5408 X-1 (Strohmayer et al. 2007; Strohmayer & Mushotzky 2009; Middleton et al. 2011a) and NGC 6946 X-1 (Rao, Feng & Kaaret 2010). While the time-scales of these quasi-periodic oscillations (QPOs) have been cited as evidence of the presence of IMBHs (Strohmayer & Mushotzky 2003, 2009; Strohmayer et al. 2007; Rao et al. 2010), Middleton et al. (2011a) have suggested a way in which such variability could be produced in the ultraluminous state. If the material in the wind is clumpy in nature (Takeuchi, Ohsuga & Mineshige 2013), then if the line-of-sight to the central regions intersects the edge of the wind the clumps will imprint stochastic variability on to the hard component by intermittently obscuring it. As the soft emission originates in the wind itself, it is not adversely affected by this mechanism (Middleton et al. 2011a; Middleton et al., in preparation).

However, this model of super-Eddington emission is not universally accepted, and other ULX models may explain the current data. Reflection models (Caballero-García & Fabian 2010) give one alternative interpretation of the energy spectrum from ULXs. These require a radiation source with a power-law-like continuum to be produced above a high spin black hole; the proponents of such models have suggested that power could be magnetically extracted from the disc and released in the emission region, thus avoiding the Eddington limit (Caballero-García & Fabian 2010). The observed ULX spectral features, including the soft excess and high energy break, are then produced by relativistically blurred reflection from the disc. Investigating the variability characteristics of ULXs provides a good test of such models – the detection of multiple spectral components, each with different variability properties, would be difficult to explain in terms of reflection. A further proposed model of ULX emission is that of slim (supercritical) discs (Abramowicz et al. 1988); these can reproduce the flat power-law spectra seen in many ULXs, and predict black hole masses in the massive stellar regime (Vierdayanti et al. 2006). However, it is not clear how variability could be produced in a slim disc alone, again providing a potential diagnostic test of such models; an additional physical issue is that slim disc spectral models neglect the wind that would be expected to arise as the accretion rate exceeds the Eddington limit (Poutanen et al. 2007; Dotan & Shaviv 2011), although later slim disc simulations do self-consistently include winds (e.g. Ohsuga & Mineshige 2011).

Here we present results from a combined X-ray spectral and timing analysis using multiple *XMM–Newton* detections of a sample of 20 ULXs with moderate- to high-quality X-ray data. We suggest a new empirical scheme to classify the ULXs by X-ray spectrum into three ultraluminous spectral types: broadened disc, hard ultraluminous and soft ultraluminous. Then, we characterize the spectral and timing properties of ULXs in each class in order to further explore and constrain models of accretion in ULXs.

2 SAMPLE SELECTION AND DATA REDUCTION

2.1 Sample selection

The primary driver of our ULX sample selection was the requirement for the data to be of high enough quality to allow us to conduct a statistically significant short-term timing analysis; as such, we defined the criteria for selecting observations based on combined European Photon Imaging Camera (EPIC) count rates and the available good time. As a starting point, we used the ULXs previously identified as those with the highest quality *XMM–Newton* data, which were subject to an in-depth spectral analysis by Gladstone et al.

(2009), and power spectral density analysis by Heil et al. (2009). In addition to these, we also considered ULXs with fluxes in excess of 5×10^{-13} erg cm^{-2} s^{-1} in the *ROSAT* High Resolution Imager (HRI) observed sample of Liu & Bregman (2005) and the *Chandra* archival sample of Swartz et al. (2004) as these are likely candidates for having reasonable quality *XMM–Newton* data, if they have been detected in previous observations. To these we added M31 ULX1 (CXOM31 J004253.1+411422; Henze et al. 2009; Kaur et al. 2012; Middleton et al. 2012), and all ULXs with a 0.3–10 keV count rate of $\gtrsim 0.3$ count s^{-1} in at least one observation in a cross-correlation of the 2XMM-DR3 (Watson et al. 2009) and the Third Reference Catalogue of Bright Galaxies (RC3; de Vaucouleurs et al. 1991) catalogues (Middleton et al., in preparation; which is an updated version of Walton et al. 2011).

We then obtained and examined all of the archival *XMM–Newton* observations of these ULXs. First, we extracted their combined EPIC count rates. Motivated by the available ULX data, it was decided to extract fractional variability from light curves with 200 s temporal binning, as a compromise between having $\gtrsim 20$ counts per bin and at least 20 temporal bins in a large sample of observations. When extracting the fractional variability we use a combined light curve from all of the available EPIC detections of the source, so we define the available good time in an observation as the sum of the 200 s bins in which all of the available detectors were on and free from high levels of background flaring. We then rejected all of the sources which did not meet the selection criteria of a minimum average 0.3–10 keV combined EPIC count rate of 0.3 count s^{-1}, in at least one *XMM–Newton* observation, and sufficient good time to extract light curves with at least twenty 200 s bins (i.e. a total of 4 ks good time), to ensure Gaussian statistics. The ULXs remaining in the sample are listed in Table 1, along with the Galactic column densities and distances to the assumed host galaxy. For the ULXs which met the sample criteria in at least one observation, we included all observations that had the same minimum good time, but met a less stringent count rate limit of at least 0.1 count s^{-1}, corresponding to an average of 20 counts per bin. In addition to full-band (0.3–10 keV) timing analysis, we also examine the properties in two other bands (0.3–1 and 1–10 keV); for this we use subsets of the observations which meet the count rate limit of ≥ 0.1 count s^{-1} in the appropriate energy band.

2.2 Data reduction

All archival *XMM–Newton* EPIC detections of the ULXs shown in Table 1 were downloaded from the NASA High Energy Astrophysics Science Archive Research Center (HEASARC) archive,[2] and those which met the criteria described in Section 2.1 were included in the subsequent work. A proprietary observation of NGC 5907 ULX also met these criteria, so was included in the analysis (Sutton et al. 2013). We summarize all the data used in our analyses in Table 2.

The data were reduced, and products extracted using standard tools in *XMM–Newton* SAS[3] (version 10.0.0). First, we extracted high energy (10–15 keV) full field light curves using EVSELECT, from which we filtered out periods subject to high background flaring, using TABGTIGEN to generate good time interval (GTI) files. When creating GTIs, we ensured that only temporally complete bins were used (i.e. no drop-outs were left in the data that could affect the

---

[2] http://heasarc.gsfc.nasa.gov/docs/archive.html
[3] http://xmm.esac.esa.int/sas/

Table 1. The ULX sample.

Source name	Reference[a]	2XMM ID	N_H [b]	Distance[c]	Reference[d]
NGC 55 ULX	1, 2, 3	2XMM J001528.8−391318	1.73	2.11	i
M31 ULX1	4, 5, 6	CXOM31 J004253.1+411422[e]	6.68	0.79	i
NGC 253 XMM2	3, 7	2XMM J004722.6−252050	1.38	3.68	i
NGC 253 ULX2	2, 7, 3	2XMM J004732.9−251749	1.38	3.68	i
M33 X-8	1	2XMM J013350.8+303937	5.69	0.92	i
NGC 1313 X-1	1, 2, 3, 7, 8	2XMM J031819.8−662911	3.95	4.39	ii
NGC 1313 X-2	1, 2, 8	2XMM J031822.1−663603	3.95	4.39	ii
IC 342 X-1	1, 3, 7, 8	2XMM J034555.6+680455	28.75	3.50	iii
IC 342 X-2	3	2XMM J034606.5+680705	28.75	3.50	iii
NGC 2403 X-1	1, 2, 3, 7, 8, 9	2XMM J073625.5+653540	4.17	3.50	i
Ho II X-1	1, 2, 3, 7, 8, 9	2XMM J081928.9+704219	3.41	3.42	ii
M81 X-6	1, 3, 8, 9	2XMM J095532.9+690034	4.22	4.27	i
Ho IX X-1	1, 2, 8	2XMM J095753.2+690348	4.26	3.61	iv
NGC 4190 ULX1	8	CXO J121345.2+363754[e]	1.62	3.47	v
NGC 4559 ULX2	1, 2, 3, 7, 8, 9	2XMM J123551.7+275604	0.80	6.98	i
NGC 4736 ULX1	3	2XMM J125048.6+410743	1.44	4.66	ii
NGC 5204 X-1	1, 2, 3, 7, 8, 9	2XMM J132938.6+582506	1.38	4.65	vi
NGC 5408 X-1	1, 2, 3, 7	2XMM J140319.6−412258	5.93	4.80	vii
NGC 5907 ULX	3, 7	2XMM J151558.6+561810	1.38	13.4	i
NGC 6946 X-1	3, 8, 9	2XMM J203500.0+601130	20.05	6.80	viii

[a]The sample sources are selected from: 1 – Gladstone, Roberts & Done (2009); 2 – Heil, Vaughan & Roberts (2009); 3 – Middleton et al. (in preparation); 4 – Henze et al. (2009); 5 – Kaur et al. (2012); 6 – Middleton et al. (2012); 7 – Walton et al. (2011); 8 – Liu & Bregman (2005); 9 – Swartz et al. (2004).
[b]Galactic column density in the direction of the source ($\times 10^{20}$ cm^{-2}), taken from Dickey & Lockman (1990).
[c]Distance to the ULX host galaxy in units of Mpc.
[d]Distances to the ULX host galaxies are taken from: i – Tully et al. (2009); ii – Jacobs et al. (2009); iii – Herrmann et al. (2008); iv – Dalcanton et al. (2009); v – Tikhonov & Karachentsev (1998); vi – Karachentsev et al. (2003); vii – Karachentsev et al. (2002); viii – Karachentsev, Sharina & Huchtmeier (2000).
[e]All *XMM–Newton* detections of M31 ULX1 and NGC 4190 ULX1 were obtained too late for these two sources to be included in the 2XMM-DR3 catalogue, so do not have a 2XMM source designation, in these cases *Chandra* source IDs are shown instead.

Table 2. Observation log.

Obs. ID[a]	Date[b]	t_{exp} [c] (ks)	Count rate[d] (count s^{-1})	θ [e] (arcmin)	Obs. ID[a]	Date[b]	t_{exp} [c] (ks)	Count rate[d] (count s^{-1})	θ [e] (arcmin)
				NGC 55 ULX					
0028740201	2001-11-14	30.4	2.0	4.40	0028740101	2001-11-15	21.4	1.1	11.25
0655050101	2010-05-24	83.0	1.1	1.13					
				M31 ULX1					
0600660201[f]	2009-12-28	16.2	5.2	2.66	0600660301[f]	2010-01-07	15.4	5.2	2.53
0600660401	2010-01-15	6.8	5.1	2.47	0600660501	2010-01-25	11.4	4.1	2.38
0600660601	2010-02-02	10.8	3.4	2.27					
				NGC 253 XMM2					
0125960101[g]	2000-06-03	34.2	0.1	5.37	0110900101	2000-12-13	7.4	0.1	4.55
0152020101	2003-06-19	38.0	0.4	5.29	0304850901	2006-01-02	9.8	0.2	3.12
0304851001	2006-01-06	9.8	0.2	3.15	0304851201	2006-01-09	18.0	0.2	3.17
				NGC 253 ULX2					
0125960101	2000-06-03	34.2	0.4	1.67	0110900101	2000-12-13	7.4	0.5	3.11
0152020101	2003-06-19	38.0	0.4	1.61	0304850901	2006-01-02	9.8	0.4	0.80
0304851001	2006-01-06	9.8	0.4	0.79	0304851201	2006-01-09	18.0	0.4	0.77
0304851301[g]	2006-01-11	6.4	0.2	0.80					
				M33 X-8					
0102640401[g]	2000-08-02	11.6	1.2	12.29	0102640101	2000-08-04	5.6	8.4	1.16
0102640701[g]	2001-07-05	10.0	1.3	12.92	0102641001[g]	2001-07-08	6.0	1.6	10.50
0102642001	2001-08-15	8.4	2.2	14.08	0102642101	2002-01-25	9.8	4.2	10.65
0102642301	2002-01-27	10.0	4.5	8.67	0141980601	2003-01-23	10.0	2.6	14.05
0141980801	2003-02-12	6.6	6.9	1.10	0141980101[g]	2003-07-11	6.2	1.6	10.62
0141980301[h]	2003-07-25	6.4	2.9	8.56	0650510101	2010-07-09	60.6	3.0	9.53
0650510201	2010-07-11	53.6	7.1	4.06					

Table 2 – *continued*

Obs. ID[a]	Date[b]	t_{exp} [c] (ks)	Count rate[d] (count s^{-1})	θ [e] (arcmin)	Obs. ID[a]	Date[b]	t_{exp} [c] (ks)	Count rate[d] (count s^{-1})	θ [e] (arcmin)
				NGC 1313 X-1					
0106860101	2000-10-17	10.4	1.1	1.45	0150280301[h]	2003-12-21	6.8	0.9	7.87
0150280601	2004-01-08	6.0	1.2	7.76	0205230301	2004-06-05	8.2	1.7	5.63
0205230501[g]	2004-11-23	15.4	0.4	7.83	0205230601	2005-02-07	4.4	0.9	7.38
0405090101	2006-10-15	77.4	1.0	1.51					
				NGC 1313 X-2					
0106860101	2000-10-17	10.4	0.4	5.44	0150280301	2003-12-21	6.8	1.4	1.02
0150280601	2004-01-08	6.0	0.6	1.04	0205230301	2004-06-05	8.2	1.5	1.26
0205230501	2004-11-23	12.6	0.5	0.99	0205230601	2005-02-07	4.4	1.5	1.10
0301860101	2006-03-06	18.2	1.0	6.17	0405090101	2006-10-15	77.4	0.9	5.40
				IC 342 X-1					
0093640901	2001-02-11	5.6	0.5	5.07	0206890201	2004-08-17	18.0	0.6	4.26
				IC 342 X-2					
0093640901[h]	2001-02-11	5.6	0.2	4.25	0206890201	2004-08-17	18.0	0.4	1.86
				NGC 2403 X-1					
0164560901	2004-09-12	56.0	0.2	5.36					
				Ho II X-1					
0112520601	2002-04-10	5.0	4.4	1.12	0200470101	2004-04-15	21.0	4.5	1.13
0561580401	2010-03-26	24.0	1.7	1.13					
				M81 X-6					
0111800101[i]	2001-04-22	77.2	0.6	3.35	0112521001	2002-04-10	7.0	0.5	11.93
0112521101	2002-04-16	8.0	0.5	11.88	0200980101[g]	2004-09-26	61.0	0.2	13.85
				Ho IX X-1					
0111800101[g]	2001-04-22	77.2	0.7	12.534	0112521001	2002-04-10	7.0	2.9	1.11
0112521101	2002-04-16	8.0	3.3	1.13	0200980101	2004-09-26	25.0	2.3	1.13
				NGC 4190 ULX1					
0654650201	2010-06-08	6.0	1.5	1.09	0654650301	2010-11-25	8.8	2.3	1.18
				NGC 4559 ULX2					
0152170501	2003-05-27	21.0	0.5	1.08					
				NGC 4736 ULX1					
0404980101	2006-11-27	37.0	0.4	2.05					
				NGC 5204 X-1					
0142770101	2003-01-06	12.0	0.8	1.13	0405690101	2006-11-15	7.6	1.7	1.10
0405690201	2006-11-19	22.0	1.5	1.08	0405690501	2006-11-25	17.0	1.0	1.13
				NGC 5408 X-1					
0112290601	2001-08-08	4.8	1.7	1.27	0112290701[g]	2001-08-24	5.6	0.7	1.23
0302900101	2006-01-13	88.0	1.2	1.09	0500750101	2008-01-13	27.3	1.1	1.06
0653380201	2010-07-17	64.2	1.5	1.12	0653380301	2010-07-19	106.2	1.5	1.12
0653380401	2011-01-26	83.4	1.4	1.11	0653380501	2011-01-28	86.2	1.4	1.07
				NGC 5907 ULX					
0145190201	2003-02-20	8.2	0.5	2.40	0145190101	2003-02-28	9.8	0.4	2.41
0673920301	2012-02-09	13.0	0.2	1.12					
				NGC 6946 X-1					
0200670101[g]	2004-06-09	4.0	0.2	1.38	0200670301	2004-06-13	8.0	0.5	1.41
0200670401[g]	2004-06-25	6.0	0.2	1.37	0500730201	2007-11-02	28.4	0.4	3.54
0500730101	2007-11-08	18.0	0.4	3.53					

[a] *XMM–Newton* observation identifiers.
[b] Observation start date, in yyyy-mm-dd format.
[c] The amount of simultaneous good time in 200 s bins, in all of the EPIC detectors used in the analysis.
[d] Combined *XMM–Newton* EPIC count rate of the ULX.
[e] Angular separation between the on-axis position of the observation and the 2XMM source position.
[f] No MOS2 detection was included in the analysis of this observation.
[g] No PN detection was included in the analysis of this observation.
[h] No MOS1 or MOS2 detections were included in the analysis of this observation.
[i] No MOS1 detection was included in the analysis of this observation.

subsequent timing analysis). The exact filtering count rate varied between observations, to maximize the utilized data whilst avoiding flaring, but typical values were $\sim$1–1.5 and $\sim$0.6 count s^{-1} for the PN and MOS detectors, respectively. When later calculating fractional variability we required that all of the available detectors were simultaneously on, so defined a GTI using the detector with the latest start time and earliest stop time. Generally this was the PN detector, except for observations with no PN detection of the ULX; here either MOS1 or MOS2 light curves were used to define the GTI.

Source spectra and light curves were mainly extracted from circular source regions with radii between 20 and 50 arcsec, with apertures at the lower end of the range being used when other sources were in close proximity to the object of interest. One exception, where neighbouring sources necessitated a very small source region radius of 12.5 arcsec, was NGC 253 ULX2. Also, in a few cases elliptical source regions were used, which were mainly necessary when the object neighboured a detector chip gap.[4] An elliptical region was also used for the MOS1 detection of M81 X-6 in observation 0112521001, where it was aligned with the direction of maximum point spread function as the source image was particularly elongated due to its large off-axis angle. One further exception was observation 0600660201 of M31 ULX1, here we followed Middleton et al. (2012), and used an annular source region to account for pile-up in the PN detection. Again following Middleton et al. (2012), we excluded the MOS2 data from the analysis of observations 0600660201 and 0600660301, as significant pile-up in these observations would have required the removal of large centroids. Count rates were low enough that pile-up was not an issue in other observations. Background spectra/light curves were extracted from circular regions; these were set equal in area to the source regions when extracting light curves, but larger regions were used when extracting spectra. Background regions were located at a similar distance from the read out node as the source, on the same or a neighbouring chip for PN detections, or on the same chip as the source for MOS detections.

Final data products were extracted using the appropriate GTI file, standard event patterns (`PATTERN` $\leq$ 4 for the PN detector, `PATTERN` $\leq$ 12 for the MOS detectors) and filters (`FLAG = 0` for spectra; `#xmmea_ep` or `#xmmea_em`, respectively, for the PN and MOS light curves). Spectra, and appropriate response matrices were extracted using XMMSELECT, then grouped using the FTOOL[5] GRPPHA; light curves were obtained using EVSELECT.

3 ANALYSIS AND RESULTS

3.1 An empirical spectral classification scheme for ULXs

The first step was to attempt to classify each of the 89 ULX observations into one of the three proposed super-Eddington spectral regimes outlined above and shown in Fig. 1. We chose to do this using a simple empirical model fit to the data, specifically a doubly absorbed multicolour disc (MCD) plus power-law model
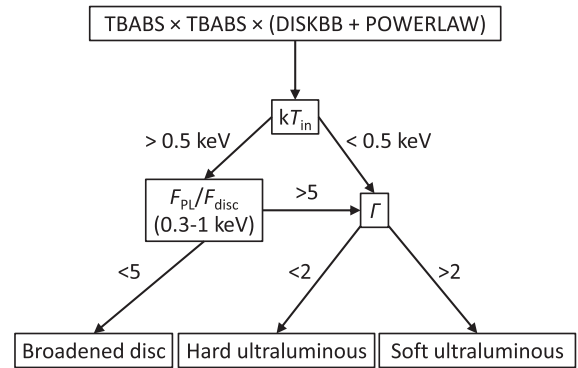
---

[4] The affected observations were the following: NGC 55 ULX – 0028740101 (PN); M33 X-8 – 0102642301 (PN, MOS1 and MOS2) and 0650510101 (PN, MOS1 and MOS2); NGC 1313 X-1 – 0150280601 (MOS1 and MOS2); NGC 1313 X-2 – 0106860101 (MOS1 and MOS2), 0301860101 (MOS1 and MOS2) and 0405090101 (MOS1 and MOS2); NGC 2403 X-1 – 0164560901 (PN); M81 X-6 – 0111800101 (PN and MOS2); NGC 6946 X-1 – 0200670301 (PN), 0500730201 (PN) and 0500730101 (PN).
[5] https://heasarc.gsfc.nasa.gov/ftools/

Figure 2. Decision tree showing the procedure by which observations were assigned into the three spectral types based on the resulting parameters from the doubly absorbed MCD plus power-law spectral model.

(CONSTANT $\times$ TBABS $\times$ TBABS $\times$ (DISKBB + POWERLAW) in XSPEC). This is motivated by the work of Gladstone et al. (2009): in their work the disc-like spectra had relatively warm discs in this model ($kT_{in} > 0.5$ keV), whereas the hard and soft ultraluminous spectra had cool discs and were themselves differentiated by their value of photon index Γ. This was $>$2 for the soft ultraluminous spectra, and $<$2 for the hard ultraluminous sources. We therefore base our classification scheme on these simple distinctions; we show the whole scheme in the form of a decision tree in Fig. 2, and discuss it further below.

In order to perform the classification, the energy spectra were grouped to a minimum of 20 counts per energy bin, to allow the spectral fitting to be carried out using χ^2 statistics in XSPEC, v12.6.0. The results of this fitting are shown in Appendix A (Table A1). The first absorption component was set equal to the Galactic value in the direction of the galaxy hosting the ULX (as per Table 1), and the latter was left free to model absorption intrinsic to the host galaxy and/or the source itself. Both components used the interstellar abundance tables of Wilms, Allen & McCray (2000). Additionally, a multiplicative constant was included to account for calibration uncertainties between the detectors, which was fixed to 1 for the PN data (or MOS1 where no PN data were available), and left free to vary for the other detectors. The constant differed by no more than 10 per cent between detectors in most cases, with the small number of exceptions being attributable to different extraction regions and/or proximity to the edge of a chip. We also extracted the 0.3–1 keV absorbed flux contributed by each of the two model components, using the CFLUX convolution model in XSPEC.[6] The ratio of these fluxes plus the best-fitting disc temperature and the photon index from the MCD plus power-law model were then used as the basis of the empirical classification scheme to diagnose the spectral state, as shown in Fig. 2.

While the classification scheme is attractive due to its simplicity, it does have limitations. One of the key diagnostics of the hard and soft ultraluminous spectra is their high energy turnover. In most cases this feature is rather subtle, so is well approximated by the power-law component in the MCD plus power-law model (cf. Fig. 1). However, in ULXs with a stronger break the simple classification

---

[6] To do this it was necessary to rearrange the spectral model such that absorption components were included separately for both the MCD and power law, which were set to be equal, i.e. CONSTANT $\times$ (TBABS $\times$ TBABS $\times$ DISKBB + TBABS $\times$ TBABS $\times$ COMPTT), with the CFLUX model component inserted before either the first or third absorption component.

scheme can break down, which notably occurs in NGC 55 ULX in the sample of Gladstone et al. (2009). In this case the power law cannot adequately approximate the strong high energy curvature, but a disc spectrum can; the two components switch places as the MCD is forced to the hard end of the spectrum, and the resulting hot disc temperature could then be naively associated with a broadened disc ULX. However, the strong soft excess in this source is then dominated by a very soft power-law component, so we can break the model degeneracy using the 0.3–1 keV flux ratio of the MCD and power law by rejecting a broadened disc interpretation where a dominant fraction of the soft emission is in the power law. The precise values chosen are motivated by NGC 55 ULX, and we include this modification in the complete classification scheme in Fig. 2. This solution seems to be sufficient to identify soft ultraluminous spectra with pronounced hard curvature, however, it is far from clear how to distinguish hard ultraluminous ULXs with pronounced curvature and little soft excess from broadened discs. A good example in this work occurs for observation 0145190101 of NGC 5907 ULX, where the best-fitting MCD plus power-law model indicates a broadened disc spectrum; however, we reject this interpretation based on a detailed multimission study of this source (Sutton et al. 2013) and use the parameters from a secondary minimum in χ^2 space to instead classify it as a hard ultraluminous spectrum. We return to this point later in Section 4.

The example of NGC 5907 ULX leads to another potential source for ambiguity: Sutton et al. (2013) find that the high absorption column in the host galaxy likely suppresses the soft excess emission, such that it is not visible in the spectrum. Such degeneracy between absorption and the intrinsic spectral shape could again be a limitation of our empirical classification scheme; for example both IC 342 X-1 and X-2 both sit behind a large Galactic absorption column, and in three out of four observations their spectral state is not constrained. As such, we further identify all highly absorbed ULX observations, and caution that the state identification in these sources is less certain. All sources with a combined column density consistent with $\gtrsim 0.5 \times 10^{22}$ cm^{-2} in the absorbed MCD plus Comptonization model (see below) were classed as highly absorbed; this model was used for this purpose in preference to the MCD plus power law, as a power-law representation of a Comptonized spectrum can become unphysical at low energies and can result in the absorption being overestimated. On this basis, high absorption was seen in all observations of IC 342 X-1, IC 342 X-2 and NGC 5907 ULX, plus observation 0200670101 of NGC 6946 X-1.

One further complication arose when fitting the MCD plus power law to the spectra from NGC 253 ULX2. This source is embedded in extended emission from the galaxy's disc and an outflow of hot gas from the starburst nucleus (Pietsch et al. 2001; Bauer et al. 2008), and initially the spectral fits were rather poor. However, the inclusion of an additional MEKAL component (with abundances frozen to solar values) to model the extended diffuse emission was able to improve this. As the MEKAL model represents emission from the hot collisionally ionized gas in the region surrounding the source, it would not be expected to vary between observations. So, we were able to constrain the spectral parameters of the hot gas by simultaneously fitting all of the observations of NGC 253 ULX2 with an invariable hot gas, plus a variable ULX model. To constrain the hot gas parameters we again used the more physically motivated ULX model, namely an MCD, plus emission from a Comptonizing corona and in this case the diffuse emission from the hot gas (CONSTANT × TBABS × (MEKAL + TBABS × (DISKBB + COMPTT)) in XSPEC). The model parameters of the MEKAL component were set to be equal in each detector for all of the observations, whilst the

other model variables[7] were allowed to vary between observations, but were set to be identical for all of the detectors in a particular observation. The multiplicative constant was fixed to 1 for the PN detector, and free to vary for the MOS detector in all of the observations. The resulting best-fitting temperature of the hot gas was $kT = 0.67^{+0.10}_{-0.05}$ keV, with a normalization of $1.5 \pm 0.3 \times 10^{-5}$ cm^{-5}, which is consistent with the models of the hotter of two plasmas identified in the central region by Bauer et al. (2008). Subsequently, we included the MEKAL emission as a fixed additive component in the spectral model for NGC 253 ULX2, both when repeating the empirical state classification and in the following spectral analysis.

The resulting spectral classifications of the ULX sample are shown in Table A1. Out of a total of 89 observations, 43 were uniquely classified as broadened discs, 15 as hard ultraluminous and 21 as soft ultraluminous. The classification of the remaining 10 observations was ambiguous, as the 1σ error bounds of the parameters were consistent with multiple spectral state identifications.

3.2 Characterizing the ULX observations using X-ray luminosity and spectral hardness

As noted above, the use of an MCD plus power-law model can create problems when extracting fluxes that are corrected for absorption given the unphysical behaviour of a power law at low energies. Therefore, in order to extract band-limited fluxes from the data, the X-ray spectra of the sample ULXs were also fitted using a second two-component spectral model – a more physical absorbed MCD plus a Comptonizing corona (CONSTANT × TBABS × TBABS × (DISKBB + COMPTT) in XSPEC). The additional advantage of this model is that cool, optically thick Comptonization can better fit the hard spectral curvature seen in many ULXs (cf. Gladstone et al. 2009). As above, a multiplicative constant and two absorption components were included in the spectral model. The coronal input soft photon temperature was set equal to the inner disc temperature; whilst this is not entirely physical, as we are not necessarily observing the intrinsic inner disc temperature, it does provide a reasonable first approximation (cf. Pintore & Zampieri 2012 and the discussion therein). This model typically resulted in acceptable fits to the majority of the ULX data. However, the limitations of the model were apparent in a small number of high-quality data sets, and it was rejected at 3σ significance in nine of the 89 observations, which notably included the five highest data quality observations of NGC 5408 X-1. A physical interpretation of the best-fitting spectral parameters is beyond the scope of the work presented here, and we just used the model to extract X-ray fluxes; we will return to this data, and in particular the features causing the poor fits in future work (Middleton et al., in preparation). Two observations of IC 342 X-2 had unconstrained disc components and were well fitted by the Comptonization model alone, so a single-component absorbed Comptonization model was used for the subsequent analysis of these data.

To characterize the X-ray spectrum seen in each of the observations, we extracted intrinsic (i.e. deabsorbed) fluxes in the full, soft and hard energy bands (0.3–10, 0.3–1 and 1–10 keV), using the CFLUX model component in XSPEC and the MCD plus Comptonizing corona model. Spectral hardness was approximated as the ratio of

---

[7] These were the extra-Galactic absorption column; both the temperature and normalization of the accretion disc; and the plasma temperature, optical depth and normalization of the corona (the input soft photon temperature was set equal to the inner disc temperature).
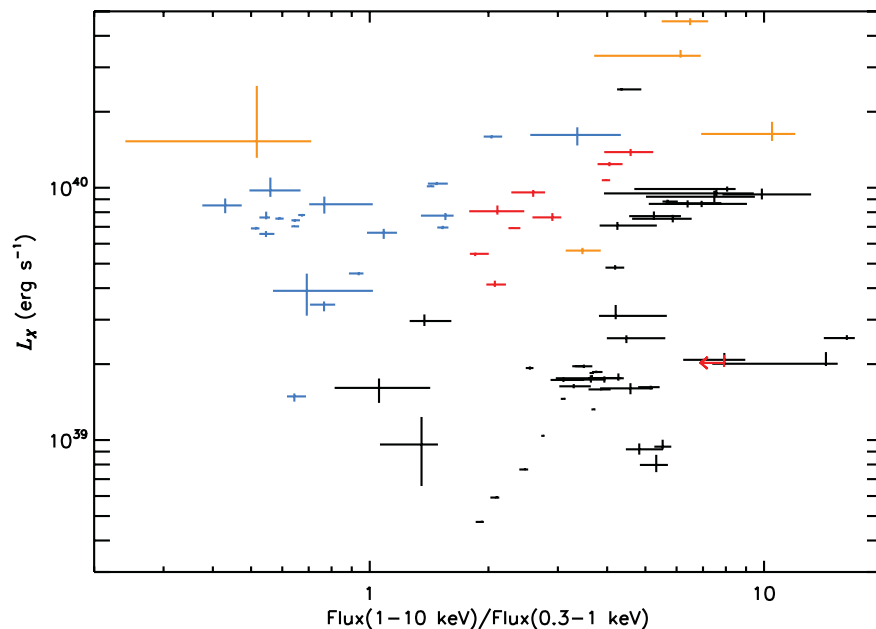
Figure 3. Hardness–luminosity diagram for the ULX sample. Spectral hardness is approximated as the ratio of the unabsorbed 0.3–1 and 1–10 keV fluxes extracted from the absorbed disc plus Comptonizing corona model, and is plotted against the 0.3–10 keV unabsorbed luminosity. The sample is split into different ULX spectral regimes, which are identified by colour: broadened discs in black, hard ultraluminous in red and soft ultraluminous in blue. Only observations with a firm spectral classification are shown. Also, any highly absorbed observations (with 1σ upper limits of $N_{\rm H} \geq 0.5 \times 10^{22}\,{\rm cm}^{-2}$) are shown in orange, as the classification scheme is less reliable in highly absorbed sources. The different spectral types of ULXs tend to occupy different regions of the diagram: few hard ultraluminous or soft ultraluminous sources are seen below $\sim 3 \times 10^{39}\,{\rm erg\,s}^{-1}$, instead below this luminosity we see mostly modified disc ULXs; the hard and soft ultraluminous sources tend to be brighter, and are generally split by spectral hardness, as would be expected given the method by which we differentiate between them.

the hard and soft band intrinsic fluxes, and 0.3–10 keV luminosities were also calculated using the full-band flux and the distances to the host galaxies from Table 1; these are shown in the form of a hardness–luminosity diagram in Fig. 3, with the observations split into the three proposed spectral types using our empirical classification method. Few hard ultraluminous and soft ultraluminous ULXs are seen below $\sim 3 \times 10^{39}\,{\rm erg\,s}^{-1}$, and the ULXs less luminous than this tend to show broadened discs. However, a few broadened discs are seen at luminosities greater than $\sim 3 \times 10^{39}\,{\rm erg\,s}^{-1}$. As expected, given that the two states are differentiated by the spectral index of the power-law tail, the hard ultraluminous sources tend to be spectrally harder than the soft ultraluminous sources, although they both seem to occupy a similar range of X-ray luminosities, with 12 out of 15 of the hard ultraluminous observations and 20 out of 21 of the soft ultraluminous observations being seen at 0.3–10 keV luminosities in the range ~ 0.3–$2 \times 10^{40}\,{\rm erg\,s}^{-1}$.

3.3 State changes in individual ULXs: ambiguous classifications or real spectral progression?

Of the 20 ULXs in the sample, 15 retained the same spectral classification throughout all of the observations included in this study when observations with an ambiguous spectral state are excluded; although four of these ULXs only had a single observation with a firm state identification, and the spectral state of IC 342 X-2 was not well constrained in any observation. However, NGC 253 ULX2, NGC 1313 X-1, Ho IX X-1, NGC 5204 X-1 and NGC 6946 ULX3 were all classified as being in two different spectral states.

NGC 253 ULX2 was observed with a disc-like spectrum in all but one observation, where it appeared with a hard ultraluminous spectrum at a similar deabsorbed 0.3–10 keV luminosity (estimated

using an absorbed MCD plus Comptonization model; see Section 3.2). In this particular case, it seems likely that it may be a case of mistaken identity, possibly due to the relatively low data quality (~ 1000 counts). When fitting the MCD plus power-law model to observation 0304851001 of NGC 253 ULX2 the best-fitting hard ultraluminous state solution had a fit statistic of $\chi^2/{\rm dof} = 181.4/168$, but there was a second local minima in χ^2 space, with a fit statistic of $\chi^2/{\rm dof} = 184.4/168$, which was instead consistent with this observation having a broadened disc spectrum.

Ho IX X-1 was observed with a hard ultraluminous spectrum in three observations, and a broadened disc in one. Unusually, the broadened disc observation occurred at the highest X-ray luminosity. In this case, the data quality is not particularly poor, and we suggest that this observation may be misclassified due to the disc-like appearance of the strong spectral curvature in a highly optically thick Comptonized spectrum (cf. the 'very thick' spectral interpretation of NGC 1313 X-1 and X-2 by Pintore & Zampieri 2012). Again, this highlights the issue in disentangling broadened discs and strongly Comptonized hard ultraluminous regime spectra.

Both hard and soft ultraluminous spectra were identified in observations of NGC 1313 X-1, NGC 5204 X-1 and NGC 6946 X-1. In the case of NGC 6946 X-1, the location of the two spectral types on the hardness–luminosity diagram appeared to be rather degenerate. In this case, we suggest that this was unlikely to be due to a real change in the spectral regime, as the spectral indices in the MCD plus power-law fits to NGC 6946 X-1 were all very close to the value of 2 used to separate the states. However, the hard ultraluminous and soft ultraluminous states in NGC 1313 X-1 and NGC 5204 X-1 do appear to clearly occupy distinct regions of hardness–luminosity space (Fig. 4); and, the soft ultraluminous spectra were only seen to occur at greater X-ray luminosities than
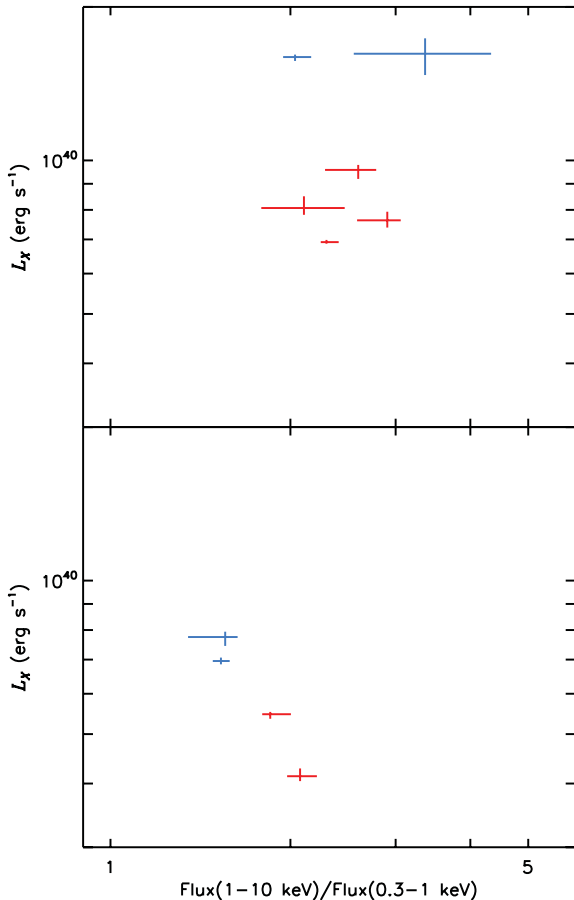
Figure 4. Hardness–luminosity diagrams, showing a subsample of the data from Fig. 3 for two individual ULXs that are seen as both hard and soft ultraluminous sources; the sources are: (top) NGC 1313 X-1 and (bottom) NGC 5204 X-1. Again, colours represent the different ultraluminous state spectral regimes: red – hard ultraluminous; blue – soft ultraluminous.

the hard ultraluminous spectra. Such spectral behaviour as observed in these two ULXs would seem to be consistent with the X-ray luminosity–spectral regime progression as originally suggested by Gladstone et al. (2009).

3.4 Short-term X-ray timing analysis

In addition to the spectral analysis detailed above, we also carried out some basic timing analysis using the diagnostic of fractional variability. Fractional variability and the associated errors were calculated following the prescription of Vaughan et al. (2003); it should be noted that this does not account for the effects of intrinsic scattering in the red noise, although Vaughan et al. state that differences in a fractional variability spectrum that are significantly larger than the estimated uncertainty would indicate achromatic variability. The main motivation behind this analysis was to provide an additional diagnostic of the spectral state, by e.g. checking for multiple variability components, and to test for consistency with the ultraluminous spectral progression suggested by Gladstone et al. (2009). In addition to the full-band (0.3–10 keV) fractional variability, we also calculated values using the energy resolved light curves in a soft (0.3–1 keV) and hard (1–10 keV) energy band. Ideally we wanted to approximate the relative variability contributions from each of the components in the two component spectrum, but it is not possible

to do this precisely, as the components overlap in energy and do not occur over the same energy range in all observations; however, whilst the detection of significantly different hard and soft fractional variabilities would not completely rule out single component spectral models (see e.g. Gierliński & Zdziarski 2005), it could provide a flag for a likely two-component spectrum with different levels of variability in each component.

To calculate fractional variability, we extracted light curves in each of the three energy bands; these were extracted with 200 s temporal binning, allowing us to probe variability on time-scales from the corresponding Nyquist frequency up to the full available good time in each observation. The resulting values of fractional variability are shown in Table A2, and similarly to the hardness–luminosity diagram (Fig. 3) above, we show the full-band fractional variabilities of ULX observations of each spectral type, plotted against spectral hardness (Fig. 5; top).

A range of variability behaviours were detected, and whilst many were consistent with upper limits of only a few per cent fractional variability (cf. Heil et al. 2009), this was not the case for all observations. Variability was detected in all three spectral classes of ULXs, although it was rather weak in the hard ultraluminous observations, where it was limited to at most ∼10 per cent. However, some soft ultraluminous observations were much more variable, having full-band fractional variabilities of up to ∼30 per cent; there were also a few highly variable detections (up to ∼40 per cent) of disc-like ULXs: observations 0125960101 and 0152020101 of NGC 253 XMM2, plus observation 0404980101 of NGC 4736 ULX1 were all inconsistent (at greater than 3σ significance) with having less than 10 per cent 0.3–10 keV fractional variability.

The high levels of variability in some of the soft ultraluminous observations were even more pronounced in the hard band (Fig. 5; bottom). Indeed, when we compare the fractional variabilities in the hard and soft energy bands (Fig. 6), it was evident that most of the variability detected in these soft ULXs was actually seen in the emission from the hard component. Intriguingly, the high levels of variability in the hard emission were not always present in the soft ultraluminous observations, rather they seem to be transient. For example, of the three observations of Ho II X-1, all of which were classified as having soft ultraluminous spectra, only one showed strong hard variability [$F_{\text{var}}(1–10 \, \text{keV}) = 21.2 \pm 0.8$ per cent; compared to <3 and 3.1 ± 0.7 per cent]. There were a few ULXs with soft ultraluminous observations in which we did not detect strong variability, these were NGC 1313 X-1, NGC 4559 ULX2 and NGC 5204 X-1 (plus IC 342 X-2; although the identification of a soft ultraluminous spectrum in this source is highly questionable). However, each of these sources was only observed with a soft ultraluminous spectrum in at most two epochs, and so had only limited opportunities for the possibly transient variability to be detected.

4 DISCUSSION

We have presented results from an X-ray spectral and timing analysis of a ULX sample, based on the highest quality available archival *XMM–Newton* data (plus a proprietary observation of NGC 5907 ULX, obtained for a different study). Now we attempt to interpret these results, with particular reference to the framework of suggested spectral progression in the super-Eddington ultraluminous state. We begin by discussing the X-ray properties seen in the sample, before attempting to interpret them in terms of models of super-Eddington accretion.
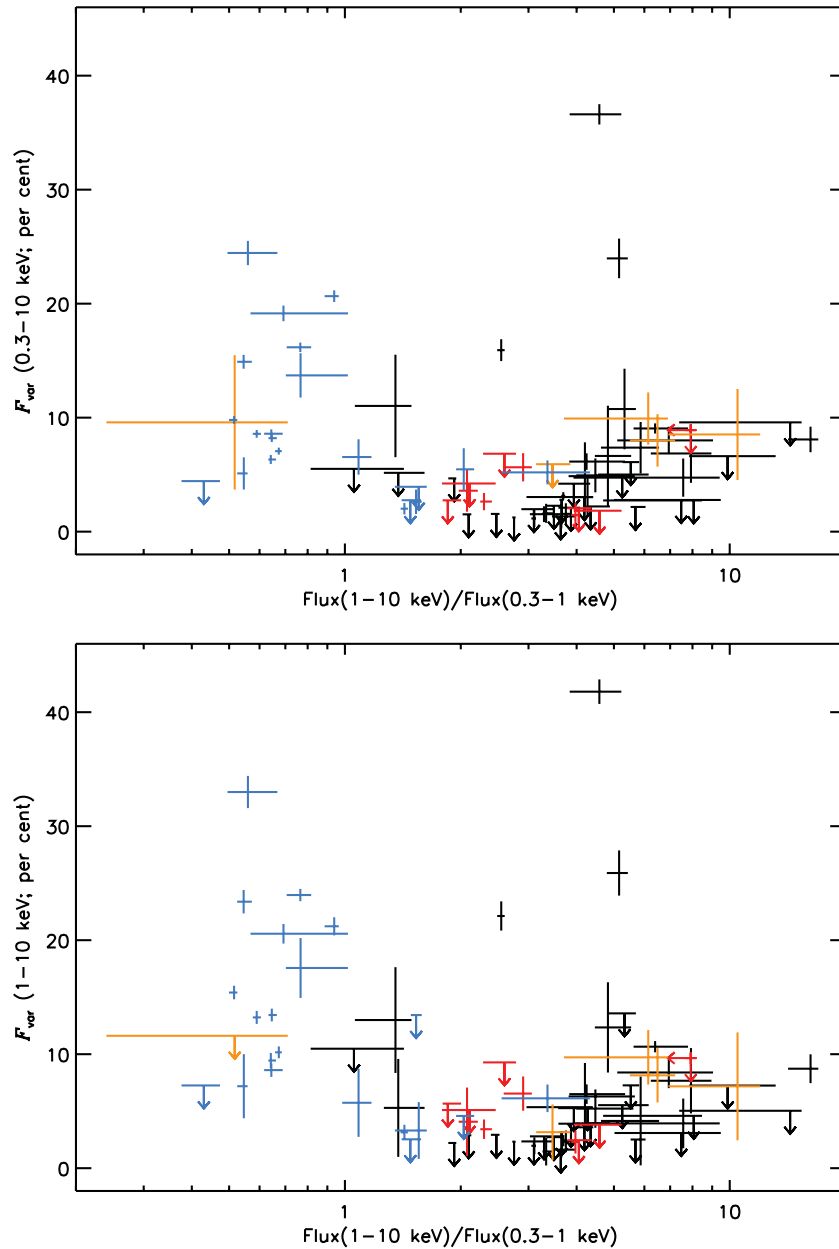
Figure 5. Full-band (top; 0.3–10 keV) and hard-band (bottom; 1–10 keV) fractional variability of the ULX sample plotted against spectral hardness. Fractional variability was calculated from light curves binned to 200 s. Errors and limits shown are at the 1σ level. The colours correspond to the three ultraluminous spectral regimes, as per previous figures: broadened discs in black, hard ultraluminous in red and soft ultraluminous in blue. Only observations with a firm spectral classification are shown. Also, any highly absorbed observations (with 1σ upper limits of $N_{\rm H} \geq 0.5 \times 10^{22}\,{\rm cm}^{-2}$) are shown in orange, as the classification scheme is less reliable in highly absorbed sources.

4.1 Interpreting the X-ray spectral and timing properties of the ULX sample

Below $\sim 3 \times 10^{39}\,{\rm erg\,s}^{-1}$ the ULX population is dominated by observations with broadened disc-like spectra. Critically, this dominant population is consistent with the suggestion from the Gladstone et al. (2009) that these sources represent accretion rates at around the Eddington limit, with the luminosity limit strongly suggestive of accretion on to sMBHs of $\lesssim 20\,{\rm M}_\odot$. However, disc-like spectra are also observed at higher X-ray luminosities in three objects (NGC 1313 X-2, M81 X-6 and NGC 4190 ULX1), up to $\sim 10^{40}\,{\rm erg\,s}^{-1}$. If these sources are indeed powered by $\sim$Eddington rate accretion, as the population of less-luminous disc-like ULXs

implies, then we are either overestimating the distance to these brighter sources, they have a higher degree of beaming than the fainter disc-like sources, or – most interestingly – we may be observing the effects of $\sim$Eddington rate accretion on to the larger MsBHs. However, it is pertinent here to again note the difficulty in distinguishing between hard ultraluminous spectra with pronounced curvature and broadened disc spectra. Given the position of these objects at the harder end of the ultraluminous regime objects in the hardness–intensity diagram, and that other ULXs observed at these luminosities appear in the super-Eddington hard ultraluminous or soft ultraluminous regimes, then the misidentification of strongly Comptonized spectra with little or no soft excess as a broadened disc should be seriously considered. So, if the apparently disc-like
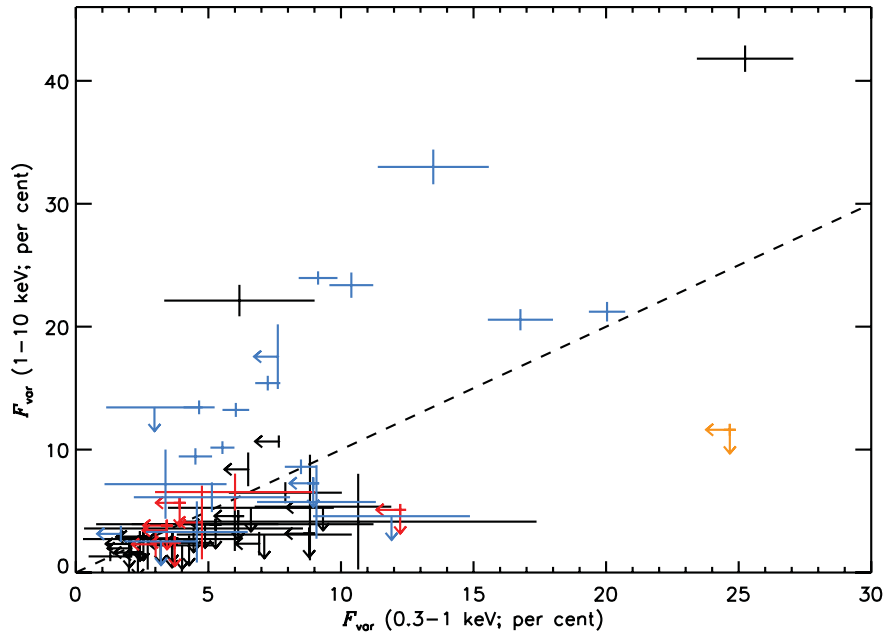
Figure 6. Hard-band (1–10 keV) fractional variability plotted against soft-band (0.3–1 keV) fractional variability for the ULX sample. The dashed line corresponds to equal values of fractional variability in each of the energy bands. Fractional variabilities were calculated from light curves with 200 s temporal binning in both energy bands. The errors and limits shown are the 1σ uncertainty limits, and the colours correspond to the spectral regimes, as per the previous figures.

ULXs above $\sim 3 \times 10^{39}$ erg s^{-1} intrinsically have hard ultraluminous spectra then MsBHs are not required, and at least this sample of ULXs can then be produced solely by $\sim$Eddington and super-Eddington accretion on to sMBHs. Clearly, future work to break this degeneracy in the classification scheme is of particular importance.

There are a number of issues in interpreting the broadened disc ULXs as standard accretion discs. Not only are they broadened, such that it can be demonstrated that they are not well fit by standard models of disc emission (cf. Gladstone et al. 2009; Middleton, Sutton & Roberts 2011b; Middleton et al. 2012), a few were also highly variable. This was the case in two observations of NGC 253 XMM2 and one of NGC 4736 ULX1. There were sufficient statistics in one observation of each source to extract a value of fractional variability in both the soft and hard energy bands; and, in each of these cases the light curve of the hard band was significantly more variable than the soft band, as is the case in the soft ultraluminous sources. If these are indeed disc spectra, then the possible origin of the variability is unclear; and it would seemingly rule out slim disc models. Rather, the variability properties would suggest that these spectra require a two-component solution, in which case the broadened disc ULXs may actually be an emerging hard/soft ultraluminous spectrum. Indeed, it has been shown that M31 ULX1 (Kaur et al. 2012; Middleton et al. 2012) and M33 X-8 (Middleton et al. 2011b), whilst both disc-like in appearance, are instead better explained as emerging two component hard/soft ultraluminous-like spectra.

The hard and soft ultraluminous regime detections are almost exclusively brighter than $\sim 3 \times 10^{39}$ erg s^{-1}. In the absence of a highly contrived distribution of black hole masses with these spectral types only occurring around more massive black holes, the lack of fainter sources in either state implies that they must be occurring at luminosities well in excess of the Eddington limit. Although both the hard and soft ultraluminous regimes are seen to occur over a similar range of X-ray luminosities, the similarities end there. The

hard ultraluminous spectra tend to be spectrally harder than the soft ultraluminous spectra, although this is not particularly surprising given that we differentiate between the two states based on the hardness of a power-law tail. Less trivial to explain is the difference in variability properties between the two states: variability in the hard ultraluminous state is rather weak and does not appear to exceed $\sim$10 per cent in any individual object (and is much lower in most), whilst much stronger variability is seen in a number of the soft ultraluminous observations. The differing variability properties support the distinctions made by our spectral classification system, but more importantly the nature of the variability can give us vital clues to the processes involved. Whilst Gladstone et al. (2009) argue that the progression to a soft ultraluminous state is characterized by the onset of a dominant spectral contribution from a soft wind, the emergent variability was observed to peak instead in the hard band. Such energy-dependent variability seems to confirm that the spectral solution must also be at least two component in nature; but it is not obvious how this could be produced using reflection models, or the accretion rate driven spectral progression originally suggested by Gladstone et al. (2009). In the latter case, the optically thick corona covering the inner disc would have to conspire to become variable in some (but not all) epochs, at around the same accretion rate that a strong wind begins to dominate the energy spectrum. This does not appear plausible. Instead, a mechanism by which ULXs with a soft ultraluminous spectrum display intermittent, strong variability of the hard component is required.

4.2 A unified model of ULX accretion

From the available evidence presented above, it seems clear that the X-ray spectral and timing characteristics of ULXs in the hard ultraluminous and soft ultraluminous regimes cannot be uniquely determined by accretion rate alone. Rather, we suggest that the key implication of this study is that it favours a model in which

both regimes are produced in a single type of system, with the observed characteristics of the source being dependent on both accretion rate and – critically – the inclination of the ULX system (cf. Poutanen et al. 2007). The required angular dependence can naturally be introduced into the ULX system by the presence of a massive outflowing, radiatively driven wind. Such a wind is expected to occur at super-Eddington accretion rates (Poutanen et al. 2007; Dotan & Shaviv 2011; Ohsuga & Mineshige 2011), indeed the supercritical accretion flow simulations of Kawashima et al. (2012) produce such a wind, and find that it takes the form of a funnel. Then, when we observe the ULX system face-on, we see down the funnel and observe emission from the innermost regions (that have a hard, cool corona/hot disc spectrum); however, at inclinations closer to the funnel opening angle, a much softer spectrum from the wind's photosphere is observed. So, at inclination angles between these, the ULX would appear with a shifting balance in the relative flux contributed from either component. In this model, the observed association between a soft spectrum and potential variability can also be achieved, if the variability can only occur at particular observation angles where the balance of component fluxes has shifted towards the wind. This is the case if the edge of the wind is clumpy in nature (cf. Middleton et al. 2011a; Takeuchi et al. 2013); then, at angles where the wind's edge intersects the line-of-sight to the central source, the clumpiness can result in variable obscuration of the hard emission region, thus extrinsically imprinting the observed, predominantly hard variability.

We argue that a unified ultraluminous state model can produce the spectral timing and properties seen in a large sample of ULXs, but for this model to be believable it is also essential that it can predict the spectral progression within individual sources. It has been predicted that an increase in the accretion rate on to a ULX would result in a narrowing of the wind's opening angle (King 2008), thus shifting the emission from the various components relative to a fixed line-of-sight. Then, a ULX could potentially transit from the hard ultraluminous state to the soft ultraluminous state with increasing accretion rate, as the wind shifts towards the observer's line-of-sight. Indeed, we observe such a spectral change in both NGC 1313 X-1 and NGC 5204 X-1. Further, we would expect to see the onset of the characteristic hard variability as the accretion rate increases still further, and the clumpy edge of the wind enters the line-of-sight; future observations of a ULX progressing through the hard ultraluminous, invariable soft ultraluminous and variable soft ultraluminous regimes could provide a strong test of this model.

The wind itself is expected to be highly ionized; we might expect to see signatures of this in the form of absorption features in ULX spectra. Walton et al. (2012) attempted to detect these using the stacked *XMM–Newton* spectra of NGC 1313 X-1 and Ho IX X-1, but found no evidence of absorption lines. However, both of these ULXs have been predominantly observed with hard ultraluminous spectra, which this work argues are likely to have clear lines-of-sight to the central emission regions, so no absorption from material in the wind is expected. Instead, the model favoured here would predict the detection of the imprint of wind absorption in soft ultraluminous ULXs; this may occur in the higher energy spectrum from the central region, or possibly across the full *XMM–Newton* bandpass if the emission from the wind is self-absorbed by the outflowing turbulent material as it becomes more diffuse and optically thin further from the source. Thus, these ULXs may display some observational similarities to high-mass X-ray binaries, that are seen through columns of $>10^{23}$ cm^{-2} of ionized stellar wind (e.g. Torrejón et al. 2010). We will revisit this in future work (Middleton et al., in preparation).

It is also interesting to consider the multiwavelength properties of ULXs in each regime. Radio nebulae have been identified around two ULXs in the soft ultraluminous state – Ho II X-1 and NGC 5408 X-1 (Kaaret et al. 2003; Miller, Mushotzky & Neff 2005; Soria et al. 2006; Lang et al. 2007). However, radio nebulae are not a unique feature of the soft ultraluminous state, one is also observed around IC 342 X-1 (Cseh et al. 2012), which is in the hard ultraluminous state; if these nebulae are inflated by disc winds, then it may further support the argument that the distinction between hard and soft ultraluminous spectra is largely due to inclination.

5 CONCLUSIONS

We have presented results from an *XMM–Newton* spectral and timing study of a sample of 20 ULXs with some of the highest quality X-ray data available. Using a new classification scheme, we separated the ULXs into three spectral types based on the results of Gladstone et al. (2009). A number of trends were identified in the spectral and timing properties of the sample, which we interpret in terms of a physical model.

(i) Below $\sim 3 \times 10^{39}$ erg s^{-1} the ULX population is dominated by broadened disc spectra. This is consistent with a population of sMBHs ($M \lesssim 20\,M_{\odot}$) accreting at close to, and just above, the Eddington limit. We therefore suggest that the broadened disc ULXs bridge the luminosity gap between the standard sub-Eddington black hole binaries and the super-Eddington ULXs with more extreme spectra. Hence, the brighter ULXs that display mainly hard ultraluminous and soft ultraluminous spectra must be at super-Eddington luminosities.

(ii) A few broadened disc ULXs were seen at higher X-ray luminosities. Rather excitingly, these could be powered by accretion on to larger black hole primaries (MsBHs). However, more mundane explanations such as higher beaming factors cannot be discounted. Alternatively, they may be misclassified objects; a hard ultraluminous spectrum with little soft excess could readily be confused with a broadened disc, in which case typical sMBHs may be sufficient to produce the entire population of ULXs up to $\sim 2 \times 10^{40}$ erg s^{-1}.

(iii) Interestingly, a few broadened disc ULXs display strong variability. Instead of being intrinsically disc like, this suggests that broadened discs may in fact be emerging two-component hard/soft ultraluminous spectra.

(iv) The brighter hard ultraluminous and soft ultraluminous ULXs differ by definition in spectral hardness, but crucially also differ in their variability properties. Low levels of variability are seen in the hard ultraluminous state (fractional variability $\ll 10$ per cent), whilst some soft ultraluminous observations are highly variable (10–30 per cent fractional variability), with the variability being strongest in the higher energy part of the spectrum (>1 keV).

(v) The observed X-ray properties can be achieved in a model with a funnel shaped wind, as is expected to emerge in super-Eddington sources. Viewed down the opening angle of the wind we observe hard emission from the central source, and so a geometrically beamed hard ultraluminous spectrum. At higher inclinations to our line-of-sight a wind-dominated soft ultraluminous spectrum is seen.

(vi) In this model, the observed hard variability in spectrally soft sources originates from the changing obscuration of the hard central emission when observed through the clumpy edge of the out-flowing wind.

(vii) If, as predicted, the opening angle of the wind narrows with increasing accretion rate, the observed spectrum can change from hard ultraluminous to soft ultraluminous at higher X-ray luminosities. This is the behaviour we see in NGC 1313 X-1 and NGC 5204 X-1.

This model is predicated on both theory and observation, and goes a long way towards unifying and explaining the X-ray characteristics of ULXs known to us from the best quality data available. But, as with any model, it requires further testing to confirm our current understanding, and develop deeper knowledge. We suggest that the key to this will be obtaining more high-quality ULX observations that constrain the spectral and timing properties of ULXs to high precision, particularly in objects that are seen to transit between different spectral regimes. However, until such observations are taken, the data presented in this paper are suggesting to us that the properties of ULXs may be explained solely by a population of sMBHs, with their different observational characteristics dependent upon two variables: their accretion rate, and their inclination angle to our line-of-sight.

REFERENCES

Abramowicz M. A., Czerny B., Lasota J. P., Szuszkiewicz E., 1988, ApJ, 332, 646
Bauer M., Pietsch W., Trinchieri G., Breitschwerdt D., Ehle M., Freyberg M. J., Read A. M., 2008, A&A, 489, 1029
Belczynski K., Bulik T., Fryer C. L., Ruiter A., Valsecchi F., Vink J. S., Hurley J. R., 2010, ApJ, 714, 1217
Caballero-García M. D., Fabian A. C., 2010, MNRAS, 402, 2559
Colbert E. J. M., Mushotzky R. F., 1999, ApJ, 519, 89
Cseh D. et al., 2012, ApJ, 749, 17
Dalcanton J. J. et al., 2009, ApJS, 183, 67
de Vaucouleurs G., de Vaucouleurs A., Corwin H. G., Jr, Buta R. J., Paturel G., Fouque P., 1991, Third Reference Catalogue of Bright Galaxies, Vols 1–3. Springer-Verlag, p. 7
Dickey J. M., Lockman F. J., 1990, ARA&A, 28, 215
Done C., Wardziński G., Gierliński M., 2004, MNRAS, 349, 393
Dotan C., Shaviv N. J., 2011, MNRAS, 413, 1623
Farrell S. A., Webb N. A., Barret D., Godet O., Rodrigues J. M., 2009, Nat, 460, 73
Feng H., Soria R., 2011, New Astron. Rev., 55, 166
Gierliński M., Zdziarski A. A., 2005, MNRAS, 363, 1349
Gladstone J. C., Roberts T. P., Done C., 2009, MNRAS, 397, 1836
Gonçalves A. C., Soria R., 2006, MNRAS, 371, 673
Heil L. M., Vaughan S., Roberts T. P., 2009, MNRAS, 397, 1061
Henze M., Pietsch W., Haberl F., Greiner J., 2009, Astron. Telegram, 2356, 1

Herrmann K. A., Ciardullo R., Feldmeier J. J., Vinciguerra M., 2008, ApJ, 683, 630
Jacobs B. A., Rizzi L., Tully R. B., Shaya E. J., Makarov D. I., Makarova L., 2009, AJ, 138, 332
Kaaret P., Corbel S., Prestwich A. H., Zezas A., 2003, Sci, 299, 365
Kajava J. J. E., Poutanen J., 2009, MNRAS, 398, 1450
Kajava J. J. E., Poutanen J., Farrell S. A., Grisé F., Kaaret P., 2012, MNRAS, 422, 990
Karachentsev I. D., Sharina M. E., Huchtmeier W. K., 2000, A&A, 362, 544
Karachentsev I. D. et al., 2002, A&A, 385, 21
Karachentsev I. D. et al., 2003, A&A, 398, 467
Kaur A. et al., 2012, A&A, 538, A49
Kawashima T., Ohsuga K., Mineshige S., Yoshida T., Heinzeller D., Matsumoto R., 2012, ApJ, 752, 18
King A. R., 2004, MNRAS, 347, L18
King A. R., 2008, MNRAS, 385, L113
Lang C. C., Kaaret P., Corbel S., Mercer A., 2007, ApJ, 666, 79
Liu J.-F., Bregman J. N., 2005, ApJS, 157, 59
Mapelli M., Ripamonti E., Zampieri L., Colpi M., Bressan A., 2010, MNRAS, 408, 234
Middleton M., Done C., Ward M., Gierliński M., Schurch N., 2009, MNRAS, 394, 250
Middleton M. J., Roberts T. P., Done C., Jackson F. E., 2011a, MNRAS, 411, 644
Middleton M. J., Sutton A. D., Roberts T. P., 2011b, MNRAS, 417, 464
Middleton M. J., Sutton A. D., Roberts T. P., Jackson F. E., Done C., 2012, MNRAS, 420, 2969
Miller N. A., Mushotzky R. F., Neff S. G., 2005, ApJ, 623, L109
Mineo S., Gilfanov M., Sunyaev R., 2012, MNRAS, 419, 2095
Miyawaki R., Makishima K., Yamada S., Gandhi P., Mizuno T., Kubota A., Tsuru T. G., Matsumoto H., 2009, PASJ, 61, 263
Ohsuga K., Mineshige S., 2011, ApJ, 736, 2
Pietsch W. et al., 2001, A&A, 365, L174
Pintore F., Zampieri L., 2012, MNRAS, 420, 1107
Poutanen J., Lipunova G., Fabrika S., Butkevich A. G., Abolmasov P., 2007, MNRAS, 377, 1187
Rao F., Feng H., Kaaret P., 2010, ApJ, 722, 620
Roberts T. P., 2007, Ap&SS, 311, 203
Roberts T. P., Warwick R. S., Ward M. J., Goad M. R., Jenkins L. P., 2005, MNRAS, 357, 1363
Soria R., 2007, Ap&SS, 311, 213
Soria R., Fender R. P., Hannikainen D. C., Read A. M., Stevens I. R., 2006, MNRAS, 368, 1527
Stobbart A.-M., Roberts T. P., Wilms J., 2006, MNRAS, 368, 397
Strohmayer T. E., Mushotzky R. F., 2003, ApJ, 586, L61
Strohmayer T. E., Mushotzky R. F., 2009, ApJ, 703, 1386
Strohmayer T. E., Mushotzky R. F., Winter L., Soria R., Uttley P., Cropper M., 2007, ApJ, 660, 580
Sutton A. D., Roberts T. P., Walton D. J., Gladstone J. C., Scott A. E., 2012, MNRAS, 423, 1154
Sutton A. D., Roberts T. P., Gladstone J. C., Farrell S. A., Reilly E., Goad M. R., Gehrels N., 2013, MNRAS, 434, 1702
Swartz D. A., Ghosh K. K., Tennant A. F., Wu K., 2004, ApJS, 154, 519
Takeuchi S., Ohsuga K., Mineshige S., 2013, PASJ, 65, 88
Tikhonov N. A., Karachentsev I. D., 1998, A&AS, 128, 325
Torrejón J. M., Schulz N. S., Nowak M. A., Kallman T. R., 2010, ApJ, 715, 947
Tully R. B., Rizzi L., Shaya E. J., Courtois H. M., Makarov D. I., Jacobs B. A., 2009, AJ, 138, 323
Ueda Y., Yamaoka K., Remillard R., 2009, ApJ, 695, 888
Vaughan S., Edelson R., Warwick R. S., Uttley P., 2003, MNRAS, 345, 1271
Vierdayanti K., Mineshige S., Ebisawa K., Kawaguchi T., 2006, PASJ, 58, 915
Walton D. J., Roberts T. P., Mateos S., Heard V., 2011, MNRAS, 416, 1844

Walton D. J., Miller J. M., Reis R. C., Fabian A. C., 2012, MNRAS, 426, 473
Watson M. G. et al., 2009, A&A, 493, 339
Wilms J., Allen A., McCray R., 2000, ApJ, 542, 914
Zampieri L., Roberts T. P., 2009, MNRAS, 400, 677
Zdziarski A. A., Grove J. E., Poutanen J., Rao A. R., Vadawale S. V., 2001, ApJ, 554, L45

APPENDIX A: ULX X-RAY SPECTRAL AND TIMING RESULTS

Here we present the parameters resulting from the MCD plus power-law spectral model fits (Table A1), and fractional variability observed in each observation (Table A2).

Table A1. Spectral parameters – TBABS × TBABS × (DISKBB + POWER-LAW).

Obs. ID[a]	χ^2/dof[b]	N_H[c]	kT_{in}[d]	Γ[e]	F_{PL}/F_{disc}[f] (0.3–1 keV)	L_X[g] (0.3–10 keV)	Spectral regime[h]
			NGC 55 ULX				
0028740201	928.9/881	0.49 ± 0.01	0.81 ± 0.02	$3.80^{+0.10}_{-0.09}$	14 ± 1	$3.4^{+0.1}_{-0.2}$	SUL
0028740101	690.2/669	$0.45^{+0.03}_{-0.02}$	0.87 ± 0.04	3.4 ± 0.2	9 ± 1	$3.9^{+0.7}_{-0.8}$	SUL
0655050101	1084.9/865	0.54 ± 0.01	0.67 ± 0.02	4.3 ± 0.08	28 ± 3	$1.49^{+0.04}_{-0.07}$	SUL
			M31 ULX1				
0600660201	1147.5/1042	0.07 ± 0.01	1.09 ± 0.01	2.7 ± 0.1	0.95 ± 0.08	$1.457^{+0.008}_{-0.007}$	Disc
0600660301	940.7/1002	$0.080^{+0.014}_{-0.009}$	$1.025^{+0.009}_{-0.009}$	$2.79^{+0.17}_{-0.09}$	$1.26^{+0.08}_{-0.09}$	1.040 ± 0.005	Disc
0600660401	995.7/977	$0.09^{+0.02}_{-0.01}$	$0.947^{+0.012}_{-0.008}$	$3.0^{+0.2}_{-0.1}$	$1.22^{+0.09}_{-0.06}$	$0.765^{+0.010}_{-0.006}$	Disc
0600660501	948.8/900	$0.11^{+0.02}_{-0.01}$	0.86 ± 0.01	$3.0^{+0.2}_{-0.1}$	1.6 ± 0.1	$0.592^{+0.008}_{-0.005}$	Disc
0600660601	871.0/857	$0.10^{+0.02}_{-0.01}$	0.80 ± 0.01	3.0 ± 0.1	$1.6^{+0.2}_{-0.1}$	$0.474^{+0.005}_{-0.003}$	Disc
			NGC 253 XMM2				
0125960101	192.7/180	$0.08^{+0.31}_{-0.04}$	$1.11^{+0.34}_{-0.07}$	1 ± 3	<0.8	$1.62^{+0.02}_{-0.03}$	Disc
0110900101	47.9/44	<0.06	$0.50^{+0.06}_{-0.05}$	$0.8^{+0.4}_{-0.9}$	$1.0^{+0.1}_{-0.2}$	$0.42^{+0.02}_{-0.03}$	Disc/HUL
0152020101	532.6/541	$0.15^{+0.03}_{-0.02}$	$1.23^{+0.09}_{-0.07}$	$2.2^{+0.3}_{-0.2}$	$1.6^{+0.3}_{-0.2}$	1.60 ± 0.08	Disc
0304850901	102.6/97	<0.3	1.4 ± 0.1	3^{+1}_{-6}	<2	$0.80^{+0.08}_{-0.05}$	Disc
0304851001	115.5/110	0.08 ± 0.05	$1.1^{+0.4}_{-0.2}$	1.5 ± 0.4	<2	$0.92^{+0.05}_{-0.04}$	Disc
0304851201	197.6/190	$0.17^{+0.10}_{-0.08}$	$1.40^{+0.08}_{-0.07}$	$2.9^{+0.9}_{-1.3}$	$0.9^{+0.3}_{-0.5}$	$0.84^{+0.06}_{-0.02}$	Disc
			NGC 253 ULX2[i]				
0125960101	597.9/581	$0.21^{+0.03}_{-0.02}$	1.52 ± 0.03	>5	$0.06^{+0.07}_{-0.02}$	$2.54^{+0.07}_{-0.04}$	Disc
0110900101	166.8/160	$0.28^{+0.04}_{-0.03}$	$1.64^{+0.07}_{-0.05}$	>6	$0.15^{+0.09}_{-0.06}$	$3.11^{+0.33}_{-0.09}$	Disc
0152020101	614.3/624	$0.33^{+0.08}_{-0.05}$	$1.69^{+0.05}_{-0.14}$	$2.2^{+0.8}_{-0.9}$	0.4 ± 0.2	$2.53^{+0.07}_{-0.11}$	Disc
0304850901	179.4/176	$0.26^{+0.03}_{-0.02}$	1.59 ± 0.05	-	0.11 ± 0.07	2.1 ± 0.1	Disc
0304851001	181.4/168	0.56 ± 0.05	$0.035^{+0.006}_{-0.007}$	$1.79^{+0.03}_{-0.05}$	3.1 ± 0.6	$2.02^{+0.15}_{-0.07}$	HUL
0304851201	319.6/287	$0.25^{+0.12}_{-0.04}$	1.52 ± 0.04	>4	$0.2^{+0.3}_{-0.1}$	$2.01^{+0.22}_{-0.04}$	Disc
0304851301	42.5/45	$0.29^{+0.06}_{-0.05}$	$1.4^{+0.2}_{-0.1}$	<10	<1	1.0 ± 0.3	Disc
			M33 X-8				
0102640401	360.4/364	$0.16^{+0.05}_{-0.03}$	1.13 ± 0.08	$2.4^{+0.4}_{-0.2}$	2.0 ± 0.3	1.84 ± 0.01	Disc
0102640101	1022.9/1035	$0.10^{+0.01}_{-0.02}$	$1.06^{+0.02}_{-0.04}$	$2.08^{+0.07}_{-0.12}$	1.2 ± 0.1	1.63 ± 0.03	Disc
0102640701	360.3/350	0.16 ± 0.02	1.0 ± 0.2	$2.1^{+0.2}_{-0.1}$	5^{+1}_{-2}	1.79 ± 0.04	Disc/HUL/SUL
0102641001	346.1/315	$0.17^{+0.04}_{-0.03}$	1.4 ± 0.1	$2.4^{+0.3}_{-0.2}$	$4.0^{+0.7}_{-0.6}$	$1.76^{+0.08}_{-0.04}$	Disc
0102642001	689.0/698	0.11 ± 0.02	0.89 ± 0.05	$1.9^{+0.1}_{-0.2}$	$1.5^{+0.4}_{-0.5}$	1.96 ± 0.03	Disc
0102642101	1078.7/1015	$0.08^{+0.02}_{-0.01}$	$1.01^{+0.04}_{-0.03}$	$1.91^{+0.11}_{-0.09}$	1.0 ± 0.1	1.86 ± 0.02	Disc
0102642301	1060.9/1049	$0.14^{+0.02}_{-0.01}$	1.10 ± 0.03	$2.33^{+0.12}_{-0.09}$	$1.6^{+0.1}_{-0.2}$	1.96 ± 0.02	Disc
0141980601	842.3/813	0.09 ± 0.02	$0.99^{+0.06}_{-0.04}$	$1.8^{+0.2}_{-0.1}$	1.1 ± 0.3	$1.73^{+0.05}_{-0.03}$	Disc
0141980801	1163.8/1018	0.11 ± 0.01	$0.88^{+0.05}_{-0.04}$	$1.94^{+0.05}_{-0.06}$	3.0 ± 0.5	$1.74^{+0.04}_{-0.05}$	Disc
0141980101	331.7/308	$0.14^{+0.04}_{-0.03}$	$0.97^{+0.12}_{-0.08}$	$2.1^{+0.3}_{-0.2}$	$2.1^{+0.4}_{-1.0}$	$1.76^{+0.03}_{-0.07}$	Disc
0141980301	539.2/500	0.06 ± 0.02	$0.96^{+0.05}_{-0.03}$	$1.9^{+0.2}_{-0.1}$	$0.9^{+0.2}_{-0.3}$	$1.59^{+0.02}_{-0.01}$	Disc
0650510101	1964.8/1658	$0.10^{+0.05}_{-0.08}$	$0.99^{+0.01}_{-0.02}$	$1.98^{+0.03}_{-0.05}$	1.18 ± 0.07	1.322 ± 0.006	Disc
0650510201	2422.2/1967	0.090 ± 0.005	1.05 ± 0.01	2.06 ± 0.03	1.08 ± 0.05	$1.789^{+0.006}_{-0.005}$	Disc

Table A1 – *continued*

Obs. ID[a]	χ^2/dof[b]	N_{H}[c]	kT_{in}[d]	Γ[e]	$F_{\mathrm{PL}}/F_{\mathrm{disc}}$[f] (0.3–1 keV)	L_{X}[g] (0.3–10 keV)	Spectral regime[h]
			NGC 1313 X-1				
0106860101	443.6/473	0.21 ± 0.02	0.26 ± 0.03	1.69 ± 0.05	1.8 ± 0.4	$7.6^{+0.3}_{-0.2}$	HUL
0150280301	271.3/254	$0.39^{+0.04}_{-0.03}$	2^{+2}_{-1}	$2.5^{+0.3}_{-0.2}$	>20	$15.9^{+0.2}_{-0.3}$	SUL
0150280601	323.6/327	0.27 ± 0.03	$0.38^{+0.05}_{-0.06}$	$1.9^{+0.1}_{-0.2}$	$1.7^{+0.5}_{-0.6}$	$11.2^{+2.8}_{-0.5}$	HUL/SUL
0205230301	574.6/601	$0.44^{+0.03}_{-0.04}$	$0.08^{+0.01}_{-0.03}$	$2.35^{+0.03}_{-0.04}$	12^{+7}_{-9}	16 ± 1	SUL
0205230501	224.9/222	0.25 ± 0.03	$0.29^{+0.05}_{-0.04}$	$1.75^{+0.09}_{-0.10}$	1.5 ± 0.3	$9.6^{+0.2}_{-0.4}$	HUL
0205230601	219.8/218	0.27 ± 0.04	$0.23^{+0.04}_{-0.03}$	$1.72^{+0.07}_{-0.08}$	1.3 ± 0.3	$8.1^{+0.4}_{-0.2}$	HUL
0405090101	1657.9/1457	0.26 ± 0.01	$0.227^{+0.009}_{-0.008}$	1.68 ± 0.02	$1.33^{+0.07}_{-0.05}$	$6.92^{+0.07}_{-0.05}$	HUL
			NGC 1313 X-2				
0106860101	167.6/185	$0.39^{+0.05}_{-0.06}$	$2.0^{+0.9}_{-0.2}$	$3.2^{+0.3}_{-0.5}$	3 ± 1	$3.0^{+0.2}_{-0.1}$	Disc
0150280301	412.2/423	0.22 ± 0.03	1.6 ± 0.3	1.7 ± 0.2	$2.8^{+0.7}_{-1.0}$	$8.6^{+0.2}_{-0.3}$	Disc
0150280601	183.1/193	0.27 ± 0.04	$1.0^{+0.4}_{-0.3}$	$2.3^{+0.1}_{-0.2}$	11^{+6}_{-10}	$3.3^{+0.2}_{-0.3}$	Disc/HUL
0205230301	546.4/580	$0.29^{+0.04}_{-0.03}$	$1.9^{+0.1}_{-0.2}$	$2.1^{+0.4}_{-0.2}$	$2.5^{+0.4}_{-0.3}$	9.9 ± 0.2	Disc
0205230501	282.2/280	0.36 ± 0.04	$2.1^{+0.5}_{-0.3}$	3.0 ± 0.3	4 ± 1	3.0 ± 0.1	Disc/SUL
0205230601	344.2/356	$0.30^{+0.12}_{-0.06}$	2.1 ± 0.1	$2.4^{+0.9}_{-0.5}$	2.1 ± 0.3	9.5 ± 0.3	Disc
0301860101	735.1/732	$0.29^{+0.06}_{-0.03}$	$1.76^{+0.08}_{-0.06}$	$2.3^{+0.5}_{-0.5}$	1.6 ± 0.2	9.2 ± 0.5	Disc
0405090101	1402.0/1484	$0.27^{+0.02}_{-0.01}$	$1.71^{+0.11}_{-0.08}$	$1.93^{+0.13}_{-0.07}$	2.9 ± 0.2	$8.7^{+0.2}_{-0.3}$	Disc
			IC 342 X-1				
0093640901	145.3/163	$0.53^{+0.15}_{-0.09}$	$0.4^{+0.2}_{-0.1}$	$1.55^{+0.09}_{-0.11}$	4 ± 3	4.4 ± 0.5	Disc/HUL
0206890201	482.0/486	$0.66^{+0.07}_{-0.06}$	$0.33^{+0.06}_{-0.05}$	1.66 ± 0.03	1.8 ± 0.4	$5.6^{+0.1}_{-0.2}$	HUL
			IC 342 X-2				
0093640901	48.9/49	$2.3^{+0.4}_{-0.2}$	2.1 ± 0.2	>-3	8^{+4}_{-5}	3.7 ± 0.2	Disc/HUL/SUL
0206890201	344.7/389	$1.8^{+0.4}_{-0.1}$	$3.2^{+0.1}_{-0.3}$	8^{+2}_{-1}	3^{+2}_{-1}	3.73 ± 0.08	Disc/SUL
			NGC 2403 X-1				
0164560901	344.6/333	$0.11^{+0.04}_{-0.05}$	$1.15^{+0.10}_{-0.09}$	$2.0^{+0.5}_{-0.3}$	<1	$1.6^{+0.1}_{-0.2}$	Disc
			Ho II X-1				
0112520601	637.9/684	0.11 ± 0.01	0.36 ± 0.02	2.38 ± 0.07	$3.3^{+1.1}_{-0.7}$	$10.4^{+0.2}_{-0.1}$	SUL
0200470101	1244.2/1118	$0.106^{+0.006}_{-0.005}$	0.34 ± 0.01	2.36 ± 0.03	$3.0^{+0.5}_{-0.2}$	10.13 ± 0.06	SUL
0561580401	846.6/753	0.098 ± 0.006	0.21 ± 0.01	2.46 ± 0.04	2.4 ± 0.3	$4.57^{+0.06}_{-0.07}$	SUL
			M81 X-6				
0111800101	1018.8/955	0.31 ± 0.03	1.42 ± 0.02	$2.8^{+0.3}_{-0.2}$	$1.7^{+0.2}_{-0.1}$	$7.1^{+0.2}_{-0.3}$	Disc
0112521001	222.3/200	$0.33^{+0.14}_{-0.07}$	$1.9^{+0.2}_{-0.1}$	$2.6^{+1.0}_{-0.6}$	$2.2^{+0.7}_{-0.5}$	$7.7^{+0.3}_{-0.2}$	Disc
0112521101	191.2/194	$0.20^{+0.10}_{-0.05}$	$1.4^{+0.4}_{-0.2}$	$1.6^{+1.4}_{-0.5}$	$1.1^{+0.5}_{-0.8}$	$7.5^{+0.3}_{-0.2}$	Disc
0200980101	413.7/397	$0.17^{+0.03}_{-0.04}$	$1.5^{+0.3}_{-0.2}$	1.5 ± 0.3	$1.3^{+0.4}_{-0.5}$	$9.4^{+0.5}_{-0.4}$	Disc
			Ho IX X-1				
0111800101	709.8/671	0.23 ± 0.02	$1.48^{+0.05}_{-0.06}$	2.2 ± 0.2	1.9 ± 0.1	24.5 ± 0.2	Disc
0112521001	832.1/819	0.15 ± 0.01	$0.31^{+0.04}_{-0.03}$	$1.65^{+0.03}_{-0.04}$	4.1 ± 0.9	12.4 ± 0.2	HUL
0112521101	829.8/874	0.187 ± 0.006	<0.01	1.83 ± 0.02	-	$13.8^{+0.4}_{-0.5}$	HUL
0200980101	1662.0/1617	$0.135^{+0.003}_{-0.006}$	0.28 ± 0.01	$1.45^{+0.01}_{-0.02}$	1.74 ± 0.09	$10.71^{+0.11}_{-0.07}$	HUL
			NGC 4190 ULX1				
0654650201	488.1/519	$0.15^{+0.07}_{-0.03}$	$1.38^{+0.07}_{-0.04}$	$2.4^{+0.6}_{-0.3}$	$1.1^{+0.3}_{-0.2}$	$4.82^{+0.11}_{-0.09}$	Disc
0654650301	718.6/752	0.13 ± 0.02	$1.5^{+0.2}_{-0.1}$	$1.66^{+0.15}_{-0.09}$	2.1 ± 0.4	8.8 ± 0.1	Disc
			NGC 4559 ULX2				
0152170501	439.5/465	0.18 ± 0.02	$0.17^{+0.02}_{-0.01}$	$2.18^{+0.04}_{-0.05}$	1.8 ± 0.3	$6.6^{+0.2}_{-0.4}$	SUL
			NGC 4736 ULX1				
0404980101	541.4/519	0.05 ± 0.02	$0.90^{+0.06}_{-0.05}$	2.2 ± 0.1	1.7 ± 0.3	1.93 ± 0.03	Disc
			NGC 5204 X-1				
0142770101	411.5/465	0.049 ± 0.009	0.26 ± 0.02	1.85 ± 0.05	2.3 ± 0.4	$4.13^{+0.15}_{-0.09}$	HUL
0405690101	665.0/572	0.10 ± 0.01	0.37 ± 0.03	2.35 ± 0.08	4 ± 1	$7.8^{+0.2}_{-0.3}$	SUL

Table A1 – *continued*

Obs. ID[a]	χ^2/dof[b]	N_H[c]	kT_in[d]	Γ[e]	$F_\mathrm{PL}/F_\mathrm{disc}$[f] (0.3–1 keV)	L_X[g] (0.3–10 keV)	Spectral regime[h]
0405690201	782.0/738	$0.102^{+0.010}_{-0.009}$	$0.36^{+0.01}_{-0.02}$	$2.22^{+0.06}_{-0.07}$	2.2 ± 0.4	7.0 ± 0.1	SUL
0405690501	626.3/610	0.053 ± 0.008	0.31 ± 0.02	$1.83^{+0.06}_{-0.07}$	1.4 ± 0.2	$5.47^{+0.06}_{-0.11}$	HUL
NGC 5408 X-1							
0112290601	297.8/317	0.02 ± 0.01	0.22 ± 0.01	2.5 ± 0.1	$0.6^{+0.2}_{-0.1}$	$7.6^{+0.4}_{-0.1}$	SUL
0112290701	106.1/138	0.05 ± 0.02	0.18 ± 0.02	2.7 ± 0.1	$1.2^{+0.3}_{-0.2}$	8.5 ± 0.6	SUL
0302900101	1166.3/930	$0.065^{+0.003}_{-0.004}$	$0.183^{+0.004}_{-0.003}$	$2.68^{+0.02}_{-0.03}$	$1.39^{+0.08}_{-0.05}$	$6.90^{+0.10}_{-0.07}$	SUL
0500750101	763.0/629	$0.077^{+0.006}_{-0.007}$	$0.179^{+0.007}_{-0.006}$	2.62 ± 0.04	1.5 ± 0.1	6.6 ± 0.2	SUL
0653380201	1448.3/1059	0.074 ± 0.004	$0.188^{+0.005}_{-0.004}$	2.55 ± 0.02	$1.54^{+0.09}_{-0.05}$	$7.03^{+0.05}_{-0.03}$	SUL
0653380301	1602.6/1126	$0.068^{+0.003}_{-0.004}$	0.194 ± 0.004	2.56 ± 0.02	$1.66^{+0.10}_{-0.06}$	$7.79^{+0.04}_{-0.11}$	SUL
0653380401	1222.5/1005	0.071 ± 0.004	$0.184^{+0.005}_{-0.004}$	$2.61^{+0.02}_{-0.03}$	$1.54^{+0.09}_{-0.05}$	$7.55^{+0.11}_{-0.06}$	SUL
0653380501	1246.3/1030	$0.061^{+0.004}_{-0.003}$	$0.194^{+0.004}_{-0.005}$	$2.47^{+0.03}_{-0.02}$	$1.26^{+0.07}_{-0.04}$	$7.43^{+0.07}_{-0.12}$	SUL
NGC 5907 ULX							
0145190201	152.1/173	$0.93^{+0.06}_{-0.05}$	0.04 ± 0.02	1.72 ± 0.05	7 ± 6	46^{+1}_{-2}	HUL
0145190101[j]	204.5/168	$1.5^{+0.2}_{-0.3}$	$0.13^{+0.02}_{-0.01}$	$1.87^{+0.08}_{-0.10}$	$0.4^{+0.3}_{-0.2}$	$33.3^{+1.8}_{-0.6}$	HUL
0673920301	141.5/135	$0.87^{+0.08}_{-0.06}$	$0.050^{+0.009}_{-0.007}$	$1.41^{+0.06}_{-0.05}$	1.8 ± 0.7	16^{+2}_{-1}	HUL
NGC 6946 X-1							
0200670101	35.8/26	$0.3^{+0.2}_{-0.1}$	$0.19^{+0.05}_{-0.04}$	$1.5^{+0.2}_{-0.4}$	$0.19^{+0.13}_{-0.07}$	15^{+10}_{-2}	HUL
0200670301	149.2/157	0.12 ± 0.04	$0.21^{+0.03}_{-0.02}$	$2.3^{+0.1}_{-0.2}$	1.0 ± 0.3	$8.6^{+0.6}_{-0.7}$	SUL
0200670401	60.3/54	<0.1	0.24 ± 0.05	$1.9^{+0.3}_{-0.1}$	0.8 ± 0.3	$8.2^{+0.9}_{-0.7}$	HUL/SUL
0500730201	425.9/406	0.20 ± 0.03	0.18 ± 0.01	$2.26^{+0.08}_{-0.07}$	0.62 ± 0.07	$9.8^{+1.2}_{-0.6}$	SUL
0500730101	290.2/273	$0.07^{+0.03}_{-0.02}$	0.23 ± 0.02	$2.05^{+0.09}_{-0.08}$	0.8 ± 0.1	$7.9^{+0.2}_{-0.4}$	HUL/SUL

Notes. Here we report the model parameters and the resulting spectral classification from fitting the ULX observations with a doubly absorbed MCD plus power-law model. Errors and limits are shown at the 1σ level, and dashes indicate an unconstrained parameter.
[a] *XMM–Newton* observation identifiers.
[b] Statistical goodness-of-fit, in terms of χ^2 and the number of degrees of freedom.
[c] Extragalactic absorption column density ($\times\,10^{22}\,\mathrm{cm}^{-2}$).
[d] Inner disc temperature in keV.
[e] Spectral index of the power-law component.
[f] The ratio of the observed 0.3–1 keV component fluxes from the power law and MCD.
[g] 0.3–10 keV deabsorbed luminosity ($\times\,10^{39}\,\mathrm{erg\,s}^{-1}$), calculated from the absorbed MCD plus Comptonization model.
[h] The resulting spectral classification of the observation, these are either broadened disc (Disc), hard ultraluminous (HUL) or soft ultraluminous (SUL).
[i] An additional MEKAL component was included in the spectral model of NGC 253 ULX2 to model extended emission in the host galaxy; this had parameters fixed to the best-fitting values from simultaneously fitting all observations with an appropriate model (TBABS $\times$ (MEKAL + TBABS $\times$ (DISKBB + COMPTT)), with a constant MEKAL component, but the parameters of the ULX model free to vary between observations.
[j] The fit reported for observation 0145190101 of NGC 5907 ULX is a local minimum in χ^2 space, with χ^2/dof $= 204.5/168$. The global minimum occurs for a $2.1^{+0.2}_{-0.1}$ keV hot disc at χ^2/dof $= 184.5/168$, which would result in the source being classified as a broadened disc during this observation. However, the combination of a hot, low-mass black hole and the extremely high luminosity of the source would require an unusually large Eddington ratio of $\sim$100, which would seem rather unphysical. The very high line-of-sight absorption column of NGC 5907 ULX, likely due to its location in an edge on spiral galaxy, may suppress the soft excess, resulting in the ambiguity in spectral classification.

Table A2. Fractional variability.

| Obs. ID[a] | F_{var}[b] | | Obs. ID[a] | F_{var}[b] | | |
	0.3–10 keV	0.3–1 keV	1–10 keV		0.3–10 keV	0.3–1 keV	1–10 keV
			NGC 55 ULX				
0028740201	16.2 ± 0.4	9.1 ± 0.7	24.0 ± 0.5	0028740101	19.1 ± 0.7	17 ± 1	20.6 ± 0.9
0655050101	8.6 ± 0.4	8.5 ± 0.6	8.6 ± 0.6				
			M31 ULX1				
0600660201	1.2 ± 0.7	<2	2.0 ± 0.7	0600660301	<1	<2	<2
0600660401	<2	<3	<3	0600660501	<2	<2	<3
0600660601	<5	4 ± 1	<2				
			NGC 253 XMM2				
0125960101	24 ± 2	$-$	26 ± 2	0110900101	<10	$-$	$-$
0152020101	36.6 ± 0.9	25 ± 2	42 ± 1	0304850901	11 ± 4	$-$	<10
0304851001	7 ± 4	$-$	12 ± 4	0304851201	<6	$-$	<7
			NGC 253 ULX2				
0125960101	8 ± 1	$-$	9 ± 1	0110900101	5 ± 3	$-$	6 ± 3
0152020101	5 ± 1	$-$	5 ± 2	0304850901	7 ± 3	$-$	8 ± 3
0304851001	<9	$-$	<10	0304851201	<10	$-$	<5
0304851301	11 ± 4	$-$	13 ± 5				
			M33 X-8				
0102640401	<3	<9	<3	0102640101	1.5 ± 0.7	<4	<3
0102640701	3 ± 2	5 ± 3	3 ± 2	0102641001	3 ± 2	9 ± 3	<5
0102642001	<2	<6	<3	0102642101	1.6 ± 0.9	<7	2 ± 1
0102642301	1.6 ± 0.8	<3	<3	0141980601	<2	<4	<2
0141980801	<1	<2	<2	0141980101	<4	7 ± 3	<5
0141980301	<2	<5	<4	0650510101	3.1 ± 0.3	4.5 ± 0.7	2.4 ± 0.5
0650510201	0.7 ± 0.5	1.3 ± 0.8	1.3 ± 0.4				
			NGC 1313 X-1				
0106860101	6 ± 1	6 ± 3	7 ± 2	0150280301	5 ± 2	12 ± 3	<5
0150280601	<5	<6	4 ± 2	0205230301	5 ± 1	5 ± 3	6 ± 1
0205230501	<7	$-$	<9	0205230601	<4	<12	<5
0405090101	2.6 ± 0.8	<3	3.4 ± 0.9				
			NGC 1313 X-2				
0106860101	<5	<9	5 ± 4	0150280301	8 ± 1	<7	8 ± 1
0150280601	4 ± 3	<8	7 ± 3	0205230301	<3	<6	<5
0205230501	<7	<8	<5	0205230601	5 ± 2	6 ± 5	4 ± 2
0301860101	<3	7 ± 3	<3	0405090101	9.1 ± 0.4	<8	10.7 ± 0.5
			IC 342 X-1				
0093640901	5 ± 3	$-$	6 ± 3	0206890201	<6	$-$	3 ± 2
			IC 342 X-2				
0093640901	<8	$-$	<8	0206890201	5 ± 2	$-$	5 ± 2
			NGC 2403 X-1				
0164560901	<6	$-$	<10				
			Ho II X-1				
0112520601	<3	3 ± 1	<3	0200470101	2.0 ± 0.5	<2	3.1 ± 0.7
0561580401	20.7 ± 0.5	20.0 ± 0.7	21.2 ± 0.8				
			M81 X-6				
0111800101	6.1 ± 0.7	8 ± 2	6.5 ± 0.9	0112521001	<5	$-$	<6
0112521101	7 ± 2	11 ± 7	<8	0200980101	<7	$-$	<7
			Ho IX X-1				
0111800101	<2	5 ± 3	<4	0112521001	<2	<4	<2
0112521101	<2	<3	<4	0200980101	<2	<3	2 ± 1
			NGC 4190 ULX1				
0654650201	<3	<9	<4	0654650301	<2	<4	<3
			NGC 4559 ULX2				
0152170501	7 ± 2	9 ± 2	6 ± 3				
			NGC 4736 ULX1				
0404980101	16 ± 1	6 ± 3	22 ± 1				

Table A2 – *continued*

Obs. ID[a]	F_{var}[b]			Obs. ID[a]	F_{var}[b]		
	0.3–10 keV	0.3–1 keV	1–10 keV		0.3–10 keV	0.3–1 keV	1–10 keV
NGC 5204 X-1							
0142770101	4 ± 2	<5	4 ± 3	0405690101	<4	5 ± 2	3 ± 2
0405690201	3 ± 1	3 ± 2	<10	0405690501	<3	<4	<6
NGC 5408 X-1							
0112290601	5 ± 1	3 ± 2	7 ± 3	0112290701	<4	<9	<7
0302900101	9.8 ± 0.3	7.2 ± 0.5	15.4 ± 0.6	0500750101	14.9 ± 0.6	10.4 ± 0.8	23 ± 1
0653380201	6.3 ± 0.4	4.5 ± 0.6	9.4 ± 0.7	0653380301	7.1 ± 0.3	5.5 ± 0.5	10.2 ± 0.5
0653380401	8.6 ± 0.3	6.0 ± 0.5	13.2 ± 0.6	0653380501	8.2 ± 0.3	4.6 ± 0.6	13.4 ± 0.6
NGC 5907 ULX							
0145190201	8 ± 2	–	8 ± 2	0145190101	10 ± 2	–	10 ± 2
0673920301	9 ± 4	–	7 ± 5				
NGC 6946 X-1							
0200670101	10 ± 6	<20	<10	0200670301	14 ± 2	<8	18 ± 3
0200670401	<8	–	12 ± 6	0500730201	24 ± 1	13 ± 2	33 ± 1
0500730101	27 ± 1	15 ± 2	35 ± 2				

[a] *XMM–Newton* observation identifiers.
[b] Fractional variability in per cent, calculated from light curves in the appropriate energy band with 200 s temporal binning. Dashes are shown for observations where fractional variability was not calculated in a particular energy band, as there were on average fewer than 20 counts per temporal bin. Errors and limits correspond to the 1σ uncertainty regions.

This paper has been typeset from a TeX/LaTeX file prepared by the author.